

# Fault Throw and Regional Uplift Histories from Drainage Analysis: Evolution of Southern Italy

J. Quye-Sawyer<sup>1</sup>, A. C. Whittaker<sup>1</sup>, G. G. Roberts<sup>1</sup>, D. H. Rood<sup>1,2</sup>

<sup>1</sup> Department of Earth Science and Engineering, Imperial College London, SW7 2AZ, UK.

<sup>2</sup> Department of Earth and Environmental Science & A. E. Lalonde AMS Laboratory, University of Ottawa, Canada.

---

This manuscript is a pre-print and has been submitted for publication in *Tectonics*. Please note that, despite having undergone peer-review, the manuscript has yet to be formally accepted for publication. If accepted, the final version of this manuscript will be available via the "Peer-reviewed Publication DOI" link on this webpage. Please feel free to contact any of the authors directly to comment on the manuscript.

---

**The accepted version of this article can be found at <https://doi.org/10.1029/2020TC006076>**

1           **Fault Throw and Regional Uplift Histories from**  
2           **Drainage Analysis: Evolution of Southern Italy**

3           **J. Quye-Sawyer<sup>1</sup>, A. C. Whittaker<sup>1</sup>, G. G. Roberts<sup>1</sup>, D. H. Rood<sup>1</sup>**

4           <sup>1</sup>Department of Earth Science and Engineering, Imperial College London, SW7 2AZ, UK.

5           **Key Points:**

- 6           • River profile inversion was used to calculate Quaternary uplift rates in space and  
7           time  
8           • Inverse modeling implies throw rate increases for Calabria's major faults  
9           • Regional uplift rates appear similar for most of Calabria once faulting is taken into  
10          account

---

Corresponding author: Jennifer Quye-Sawyer, [jennifer.quye-sawyer11@imperial.ac.uk](mailto:jennifer.quye-sawyer11@imperial.ac.uk)

**Abstract**

Landscapes can record elevation changes caused by multiple tectonic processes. Here we show how coeval histories of spatially coincident normal faulting and regional uplift can be deconvolved from river networks. We focus on Calabria, a tectonically active region incised by rivers containing knickpoints and knickzones. Marine fauna indicate that Calabria has been uplifted by  $>1$  km since approximately 0.8–1.2 Ma, which we used to calibrate parameters in a stream power erosional model. To deconvolve the local and regional uplift contributions to topography, we performed a spatio-temporal inversion of 994 fluvial longitudinal profiles. Uplift rates from fluvial inversion replicate the spatial trend of rates derived from dated Mid–Late Pleistocene marine terraces, and the magnitude of predicted uplift rates matches the majority of marine terrace uplift rates. We used the predicted uplift history to analyse long-term fault throw, and combined throw estimates with ratios of footwall uplift to hanging wall subsidence to isolate the non-fault related contribution to uplift. Increases in fault throw rate—which may suggest fault linkage and growth—have been identified on two major faults from fluvial inverse modeling, and total fault throw is consistent with independent estimates. The temporal evolution of non-fault related regional uplift is similar at three locations. Our results may be consistent with toroidal mantle flow generating uplift, perhaps if faulting reduces the strength of the overriding plate. In conclusion, fluvial inverse modeling can be an effective technique to quantify fault array evolution and can deconvolve different sources of uplift that are superimposed in space and time.

**1 Introduction**

The evolution of normal faults has important implications for long-term seismic hazard, and changes in topography during the development of a fault array impact upon a range of factors including plate rheology and sediment routing (e.g. Li et al., 2016; Marc et al., 2016; Cowie et al., 2017). Techniques such as trenching and cosmogenic dating of fault scarps can constrain fault throw rates over timescales of  $\sim 10^2$ – $10^3$  years and can successfully estimate earthquake recurrence intervals (e.g. Pantosti et al., 1993; G. P. Roberts & Michetti, 2004; Cowie et al., 2017). Fault throw over longer timescales ( $>10^3$  years) can be investigated using stratigraphic data and structural cross sections (e.g. Mirabella et al., 2011; Ford et al., 2013; Shen et al., 2017), however a complete temporal and spatial record of throw rates may be limited by the absence of datable stratigraphy.

Fortunately, fluvial networks provide an opportunity to overcome these limitations and constrain throw rate on the length and timescales that may be pertinent to the development of a fault array, i.e.  $\sim 10^2$ – $10^5$  m and  $\sim 10^4$ – $10^7$  years (e.g. Cowie et al., 2000; McLeod et al., 2000). Quantitative fluvial erosion models can elucidate tectonic changes without necessarily relying upon the stratigraphic archive, signifying their importance in low–mid latitude terrestrial settings where fluvial landscapes are ubiquitous. The morphology and erosion rates of individual rivers have been used to confirm the location of active faults, estimate increases in throw rate, and understand fault interaction or relay ramp development (e.g. Commins et al., 2005; Hopkins & Dawers, 2015). These studies have successfully shown that drainage morphology is sensitive to the evolution of individual fault strands. Nonetheless, active faulting rarely occurs in isolation from other tectonic processes (e.g. mantle flow, plate flexure, isostatic rebound), which often modify topography over larger spatial scales (e.g.  $10^5$  m). Therefore, separating the effect of faulting from the other factors that generate topography remains a wider challenge in tectonic and geomorphic research.

**1.1 Spatial scales of uplift and geomorphic response**

Observational and theoretical studies have demonstrated the influence of tectonic perturbations on the morphology of fluvial networks (e.g. Howard, 1994; Stock & Montgomery, 1999). In particular, longitudinal profiles (i.e. plots of channel elevation as a func-

tion of downstream distance) usually exhibit a transient response to changes in uplift rate in the form of breaks in slope, known as knickpoints (e.g. Whipple & Tucker, 1999; Kirby & Whipple, 2012). Rivers are particularly useful for tectonic analysis because, for a particular upstream area, higher uplift rates produce steeper channel slopes (assuming constant sediment cover, precipitation etc.), therefore spatial differences in uplift magnitude may be observed directly from the landscape (e.g. Kirby & Whipple, 2012; Whittaker, 2012). Second, river erosion in detachment-limited settings is dominantly an advective process. As the wave of erosion travels upstream through time (assuming erosion rate is linearly proportional to channel slope) the river contains a record of past uplift events (e.g. Loget & Van Den Driessche, 2009; Pritchard et al., 2009; G. G. Roberts & White, 2010).

Changes in uplift rate estimated from river profiles have been used to examine causative tectonic processes such as active faulting, fold growth or dynamic topography (e.g. Kirby & Whipple, 2001; G. G. Roberts & White, 2010; Boulton et al., 2014; Whittaker & Walker, 2015). Some work has focussed on long-wavelength processes by inverting large numbers of river profiles to find continent or island-wide uplift histories (e.g. G. G. Roberts et al., 2012; Czarnota et al., 2014; Fox et al., 2014; Paul et al., 2014; Rodríguez Tribaldos et al., 2017), while other studies have investigated smaller scale phenomena (e.g. Goren et al., 2014; Quye-Sawyer et al., 2020). This analysis is the first to quantitatively deconvolve long wavelength ‘regional’ uplift and short wavelength faulting using river profile inversion.

Geophysical and geomorphological studies suggest that Italy’s topography has been generated by active faulting and longer wavelength processes, probably associated with sub-lithospheric support (e.g. d’Agostino et al., 2001; Faure Walker et al., 2012; Faccenna et al., 2014). However, how different processes have contributed to the formation of topography remains largely unknown, and the rates and magnitudes of each process are poorly quantified throughout the region. The aim of this paper is to investigate faulting and longer wavelength regional uplift in Calabria where geomorphological and archaeological observations, and geochronological data, help to constrain landscape evolution over a range of length and timescales (Westaway, 1993; Ferranti et al., 2006; Stanley & Bernasconi, 2012; Pirrotta et al., 2016). We use these data alongside 994 river profiles, which cross all major faults in Calabria, and employ a simple stream power relationship to invert their longitudinal profiles for a spatio-temporal uplift history. We show that Calabria’s rivers record both regional uplift and changes in fault throw rate.

## 1.2 Geology and geomorphology of Calabria

The Cretaceous to Eocene collision of the Eurasian and African plates, which resulted in the Alpine and Pyrenean orogenies in Western Europe, caused profound changes to the landscape of the Mediterranean region. The subsequent segmentation of the Alps, accompanied by significant block rotations and magmatism (e.g. Rosenbaum et al., 2002; Savelli, 2002), created positive and negative changes in landscape elevation on geologic and historical timescales (e.g. Braga et al., 2003; Fellin et al., 2005; Ferranti et al., 2008; Scicchitano et al., 2008; Antonioli et al., 2009). However, the extent to which the present-day topography of Southern Italy records crustal stresses, plate flexure, mantle processes or climate change is poorly understood.

The geology of Calabria reveals the dramatic paleogeographic change of southwest Europe since Late Eocene–Oligocene cessation of Alpine compression. Its basement of granites, gneisses and schists (Figure 1), which were deformed during the Variscan orogeny, indicate that Calabria was positioned on the Eurasian margin prior to Alpine collision (Rossetti et al., 2001, 2004; Rosenbaum et al., 2002). Metamorphosed ophiolites in the Alpine Nappes (Figure 1) and high pressure–low temperature metamorphism imply that the region was proximal to the subduction front during the closure of Tethys (e.g. Liberi et al., 2006; Pezzino et al., 2008), with localised compression until the Pliocene (Capozzi et al., 2012).

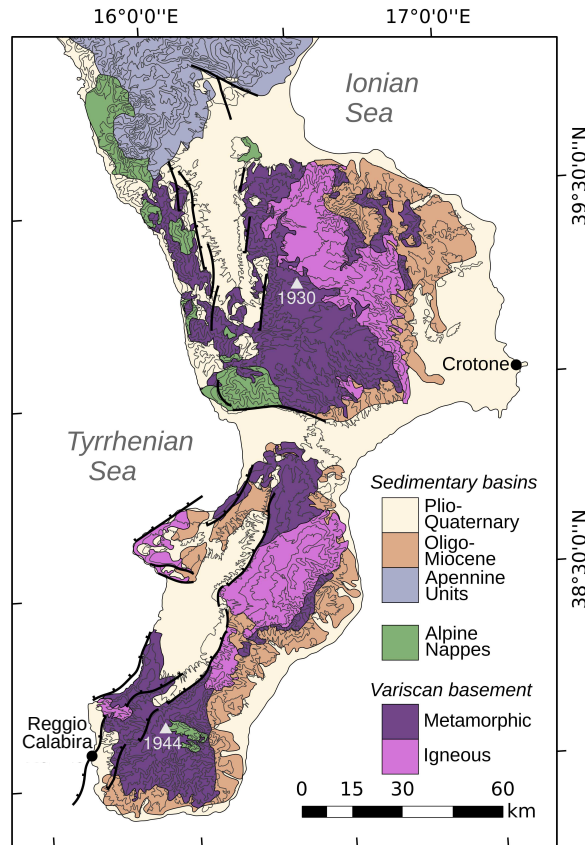


**Figure 1.** Simplified geological map of Calabria. Bedrock geology modified from Monaco and Tortorici (2000); Catalano et al. (2008); Minelli and Faccenna (2010); Fiannacca et al. (2015). Topographic contours at 250 m intervals, with spot elevations (grey triangles) of peaks in the Sila and Aspromonte massifs in metres. Active fault traces shown as black lines, with ticks on hanging wall.

115 The southern Tyrrhenian Sea has rapidly stretched since the late Miocene separation of Sardinia and Calabria, and ages of dredged oceanic crust reveal episodic oceanic  
 116 spreading (Rosenbaum & Lister, 2004). Seismic tomography and deep seismicity (35 to  
 117 500 km) indicate that the Tethyan oceanic plate still subducts beneath Calabria (e.g.  
 118 Piromallo & Morelli, 2003; Chiarabba et al., 2005). An offshore accretionary prism is observed  
 119 in seismic data from the Ionian Sea (Minelli & Faccenna, 2010). In contrast, active  
 120 extension is present both onshore Calabria and along its Tyrrhenian coastline, dominantly  
 121 expressed as a series of NNE–SSW striking normal faults (Figure 2; e.g. Catalano  
 122 et al., 2008). Numerous historical earthquakes (Figure 3b), many with devastating  
 123 tsunamis, attest to the recent activity of the majority of these faults (e.g. Catalano et  
 124 al., 2008; Meschis et al., 2019). This close spatial coupling of compression and extension  
 125 is also observed further north in the Italian Apennines and is attributed to the roll-back  
 126 of the cold subducting slab of the Tethyan oceanic plate (Malinverno & Ryan, 1986).  
 127

128 However, despite numerous observations of recent crustal extension, marine terraces  
 129 and exposed tidal notches show that much of Calabria has experienced rapid Quater-  
 130 nary uplift (Antonioli et al., 2009). Shear wave anisotropy measurements are consistent  
 131 with mantle convection around the subducting plate (e.g. Civello & Margheriti, 2004;  
 132 Baccheschi et al., 2008), which has been recently suggested as the cause of Calabria’s long

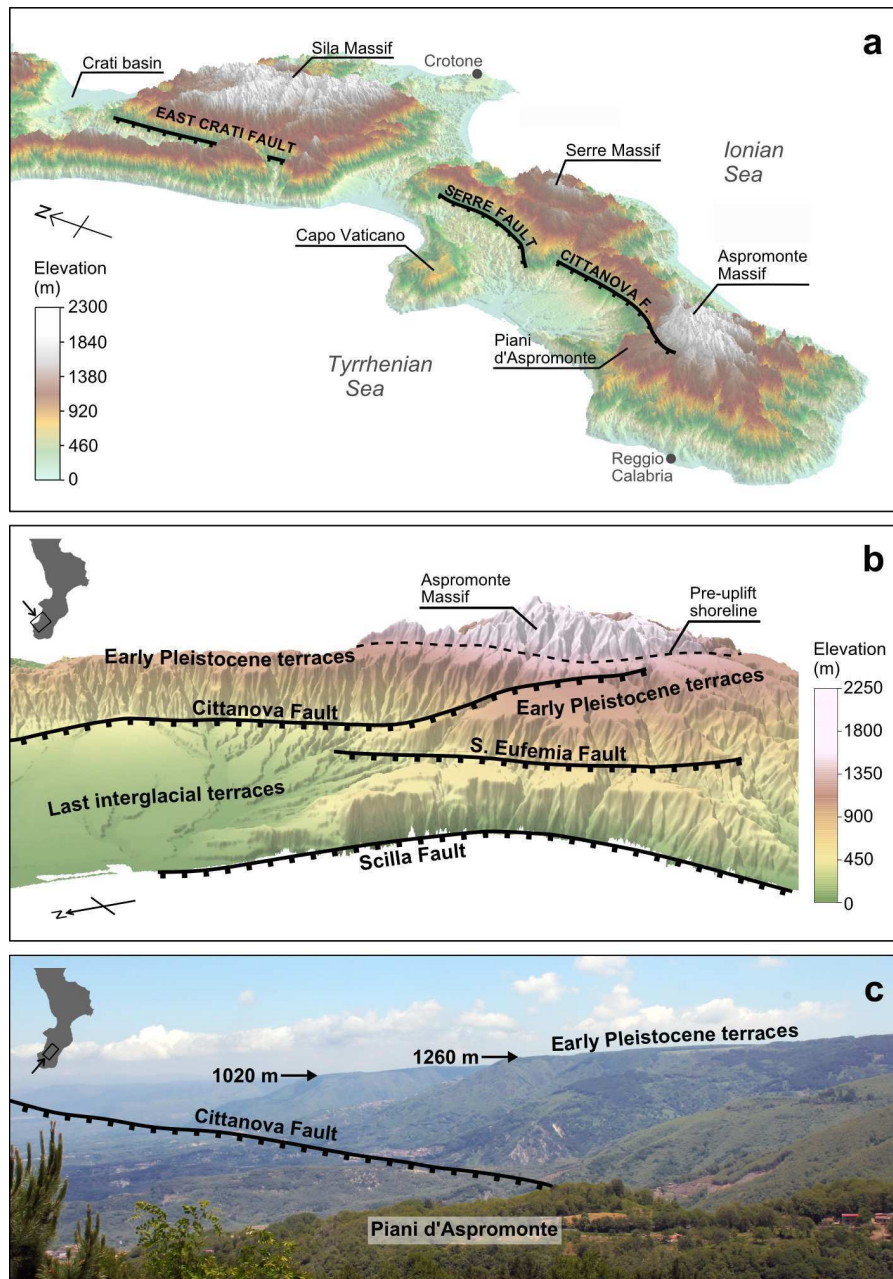


**Figure 2.** Geomorphologic expression of active normal faults and marine terraces in Calabria. (a) Perspective view of SRTM DEM with 2× vertical exaggeration. Selected geomorphic features and major faults labelled. (b) SRTM DEM with 1.75× vertical exaggeration, focussed on Aspromonte region. Visual extent and viewing direction shown by box and arrow on inset map. (c) Photograph of the Cittanova fault, facing northeast. Arrows on photograph indicate locations of footwall crests.

133 wavelength uplift (Faccenna et al., 2014; Magni et al., 2014), though little work to date  
 134 has focused on isolating rates of regional uplift from dynamic mantle processes.

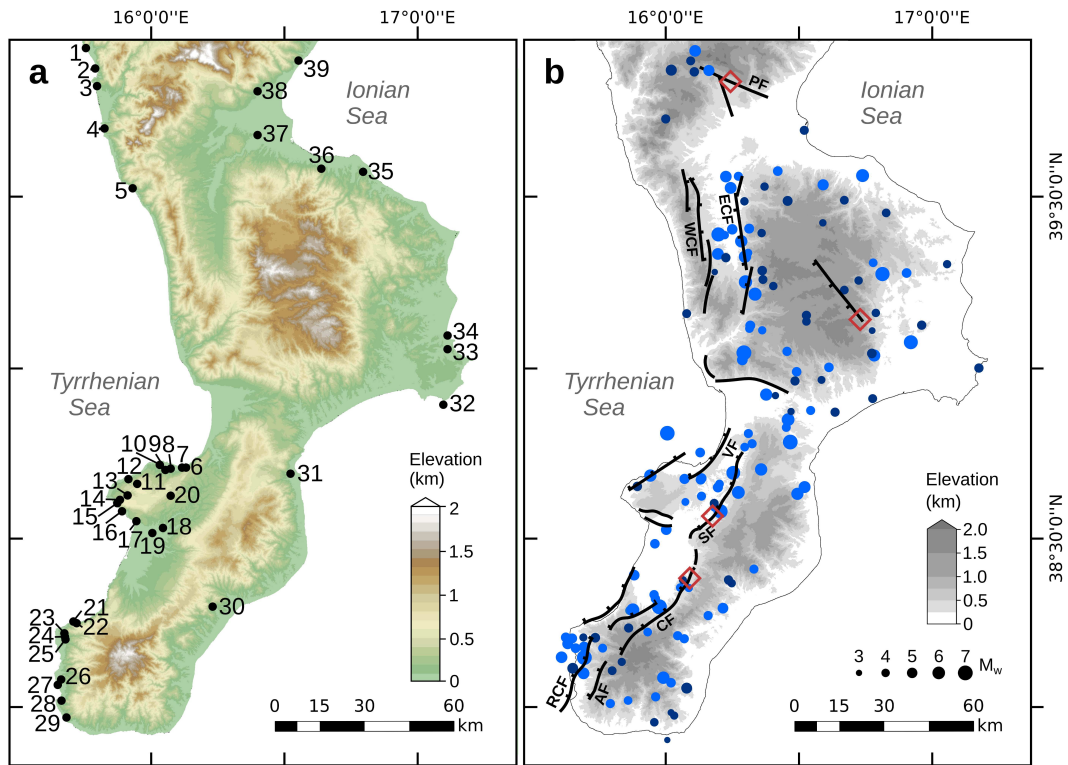


**Figure 3.** Calabria’s marine terraces and historical / paleoseismicity. (a) Locations of Pleistocene–Recent marine terraces reported in literature (for reference to ID numbers see Table 1). (b) Earthquake epicentres from the INGV 2015 seismic catalogue. Only earthquakes reported at >2 locations in the catalogue are included in this Figure to ensure robust triangulation of earthquake epicentres. Pre- 1970: light blue circles. Post- 1970: dark blue circles. Red diamonds: dated trenching sites (Galli et al., 2008). PF: Pollino fault; WCF: West Crati fault; ECF: East Crati Fault; VF: Vibo fault; SF: Serre fault; CF: Cittanova fault; AF: Armo fault; RCF: Reggio Calabria fault.

135

### 1.2.1 Geomorphic observations of Quaternary uplift

136

137

138

139

140

141

142

143

144

145

146

147

148

149

150

151

Early Pleistocene marine terraces reach heights of 1.3 km above sea-level in the Aspromonte region of southern Calabria (Figure 2). These marine terraces, the oldest in the region and the only terraces found in the footwalls of the major faults, are poorly dated with reported ages between 0.58–1.8 Ma (e.g. Tortorici et al., 1995; Catalano et al., 2008; Roda-Boluda & Whittaker, 2017). However, a probable age is the Sicilian Stage (0.8–1.2 Ma), based primarily on the first appearance of ‘boreal guests’ including *Artica islandica* and *Hyalinea balthica* (e.g. Miyauchi et al., 1994). The oldest terraces are easily identified by their well-preserved wave cut platforms flanking the higher relief massifs (Miyauchi et al., 1994; Roda-Boluda & Whittaker, 2017). The widespread nature of these marine terraces demonstrate that the majority of Calabria’s topography has probably developed since the Sicilian Stage and indicate that much of the region was below sea-level prior to this time. The massifs of weathered Paleozoic crystalline basement (with peaks  $\approx$ 1.8 km above sea-level) are interpreted to have been an archipelago of small islands, surrounded by deltas and separated by tidal straits, that were exposed above sea-level before the initiation of Pleistocene uplift (e.g. Westaway, 1993; Longhitano, 2011; Longhitano et al., 2012; Rossi et al., 2017).

Last-interglacial (MIS 5e) tidal notches and marine terraces are identified along Calabria's coastline due to the presence of *Strombus bubonius* and other warm-water 'Senegalese' fauna, U/Th ages and aminoacid racemization correlation (Figure 3a; Table 1). Tectonic uplift rates can be calculated from marine terraces using

$$U = \frac{H_t - S_H}{\Delta t} \quad (1)$$

152 where  $U$  is uplift rate,  $H_t$  is the observed elevation of the marine terrace,  $S_H$  is the relative  
 153 sea-level at the time of terrace formation (where positive values of  $S_H$  denote sea-  
 154 levels higher than present) and  $\Delta t$  is the time since terrace formation (e.g. Ferranti et  
 155 al., 2006). The heights of last interglacial terraces are highly variable across Calabria,  
 156 with the highest uplift rates ( $>2.5 \text{ mm yr}^{-1}$  for the last 124 ka) observed in footwalls  
 157 of faults on the Capo Vaticano peninsula (Bianca et al., 2011). Lower uplift rates (0.47  
 158 to  $0.89 \text{ mm yr}^{-1}$  for the last 124 ka) exist in the adjacent, and relatively subsiding, hang-  
 159 ing wall of the Cittanova fault (Table 1 and Figure 3). Terrace heights in the Crotona  
 160 Basin,  $>50 \text{ km}$  from major active faults, are indicative of consistently low uplift rates  
 161 ( $<1 \text{ mm yr}^{-1}$ ; Table 1: ID 32 to 34). Holocene uplift rates show similar spatial variabil-  
 162 ity to the Late Pleistocene rates and may imply a temporal increase in uplift rate near  
 163 the Messina Strait (Antonioli et al., 2006).

164 Unfortunately, absolute ages of older terraces are scarce across much of Calabria.  
 165 Optically Stimulated Luminescence dating of 125–380 m elevation marine terraces on  
 166 the Capo Vaticano peninsula yielded ages of  $184 \pm 20 \text{ ka}$  to  $214 \pm 25 \text{ ka}$ , correspond-  
 167 ing to highstands within MIS 7 (Figure 3; Table 1 Bianca et al., 2011). The presence of  
 168 higher, though currently undated, terraces on Capo Vaticano mean that these observa-  
 169 tions are consistent with uplift initiating prior to 200 ka in this area (Bianca et al., 2011).  
 170 Isolated marine terraces mapped in northern Calabria (e.g. Isola di Dino) do not have  
 171 robust absolute age constraints (see Table 1; Figure 3: ID 1–5, 38–40), and, as such, dif-  
 172 ferent ages have been attributed to the same terrace (Carobene & Dai Pra, 1990; West-  
 173 away, 1993). In general, the superposition of normal faulting and regional uplift com-  
 174 plicates terrace correlation across Calabria, and the uneven distribution of uplift con-  
 175 straints can make it difficult to fully quantify fault growth or regional uplift.

176 Several local studies show that Calabria's rivers have transient longitudinal pro-  
 177 files containing at least one knickpoint (e.g. Pirrotta et al., 2016; Roda-Boluda & Whit-  
 178 taker, 2017; Robustelli, 2019), which also suggests that uplift has varied both spatially  
 179 and temporally across the region. Catchment averaged erosion rates derived from cos-  
 180 mogenic nuclide concentrations are similarly variable. Erosion rates are generally low at  
 181 high elevations within the massifs or above fluvial knickpoints ( $\sim 0.1 \text{ mm yr}^{-1}$ ), and are  
 182 higher (up to  $1.6 \text{ mm yr}^{-1}$ ) upstream of active faults or in small catchments close to the  
 183 coast below a major knickpoint (Cyr et al., 2010; Olivetti et al., 2012; Roda-Boluda et  
 184 al., 2019).

### 185 **1.2.2 Active faults in Calabria**

186 Over 130 moderate to large magnitude earthquakes ( $3.1 \leq M \leq 7.1$ ) with well-  
 187 constrained epicentres have been documented throughout Calabria in the last ca. 1000 yr  
 188 (Rovida et al., 2016). The wide spatial distribution of their epicentres indicates the pres-  
 189 ence of many active faults (Figure 3b). Radiocarbon dating of trenched normal faults  
 190 and damage to archaeological sites provides evidence for Holocene activity of some struc-  
 191 tures (Galli & Bosi, 2002; Galli et al., 2007; Cinti et al., 2015). Many of Calabria's faults  
 192 have a clear geomorphic expression that can be mapped from digital elevation models  
 193 (Figure 2), and the large fault scarps imply that seismicity originated during the Pleis-  
 194 tocene (e.g. Monaco & Tortorici, 2000; Catalano et al., 2008). Major faults pertinent  
 195 to this study will be discussed in detail below.

196 The NW dipping NE–SW striking Cittanova fault lies entirely onshore, and has the  
 197 longest fault trace ( $\sim 42 \text{ km}$ ) in Calabria (Catalano et al., 2008). With fault segments  
 198 of  $\sim 10 \text{ km}$ , the Cittanova fault probably reached its current size through the interaction



**Table 1.** Calabria’s marine terraces and tidal notches with minimum–maximum average uplift rates since time indicated in the age column. Elevation errors from Ferranti et al. (2006). Uplift rates calculated using Equation 1 assuming MIS 5e occurred during 120–130 ka, with sea-level 3–9 m above that of the present day (Ferranti et al., 2006). Paleosea-levels and durations of other highstands from Siddall et al. (2007) and Siddall et al. (2010). Dating method: TL = Thermoluminescence; OSL = Optically stimulated luminescence; SB = *Strombus bubonius*; SF = Senegalese fauna (not *S. bubonius*); RC = Radiocarbon (calibrated age used); U/Th = U-series or U/Th-series; AM = Amminoacid racimization. Assume terrace correlation if no dating method is given. References: [1] Antonioli et al. (2006); [2] Bianca et al. (2011); [3] Cucci (2004); [4] Cucci and Cinti (1998); [5] Ferranti et al. (2006); [6] G. P. Roberts et al. (2013).

ID	Long. (°)	Lat. (°)	Highstand	Age (ka)	Dating method	Elevation (m)	Uplift rate (mm yr <sup>-1</sup> )	Ref.
1	15.750	39.933				9.5 ± 0.1		5
2	15.785	39.874				7 ± 0.1		5
3	15.792	39.823				8 ± 8		5
4	15.820	39.700				10 ± 0.1		5
5	15.926	39.526				12 ± 0.1		5
6	16.127	38.708	MIS 7a	184 ± 20	OSL	125	0.68–0.72	2
7(a)	16.112	38.708	MIS 5e	130 ± 8	SB, U/Th	52 ± 20	0.18–0.58	5
7(b)	16.112	38.708	MIS 5e	121 ± 7	SB, U/Th	50 ± 20	0.16–0.56	5
7(c)	16.106	38.707	MIS 5e	132 ± 1.6; 142 ± 1.8	U/Th	50	0.32–0.39	6
8	16.069	38.705	MIS 5e	134 ± 13	TL	153 ± 20	0.95–1.42	5
9	16.049	38.701	MIS 5e	128 ± 13	TL	140 ± 20	0.93–1.39	5
10	16.028	38.716	MIS 5e		TL	216 ± 20	1.44–1.94	5
11	15.943	38.660	MIS 7c	207 ± 22	OSL	560	2.48–2.81	2
12	15.910	38.674	MIS 5c	94 ± 8	OSL	52	0.63–0.73	2
13	15.907	38.626	MIS 7c	199 ± 21	OSL	465	2.19–2.32	2
14	15.878	38.613	MIS 5e		SF	285 ± 20	1.97–2.52	5
15	15.868	38.603				120 ± 20		5
16(a)	15.886	38.579	Holocene	5.358 ± 0.1	RC	1.8		1
16(b)	15.886	38.579	Holocene	5.667 ± 0.08	RC	1.8		1
17	15.940	38.550	MIS 5e		SB	90 ± 20	0.47–0.89	5
18	16.040	38.530	MIS 5e		SB	65 ± 4	0.40–0.55	5
19	16.000	38.515	MIS 3c	62 ± 6	OSL	50		2
20	16.069	38.625	MIS 7e	214 ± 25	OSL	380	1.55–1.80	2
21(a)	15.703	38.253	Holocene	3.318 ± 0.103	RC	2.9		1
21(b)	15.703	38.253	Holocene	3.901 ± 0.105	RC	2.9		1
21(c)	15.703	38.253	Holocene	2.665 ± 0.164	RC	2.5		1
21(d)	15.703	38.253	Holocene	2.37 ± 0.105	RC	2		1
22	15.715	38.248				125 ± 20		5
23	15.669	38.218				143 ± 20		5
24	15.671	38.208				170 ± 20		5
25	15.673	38.200	MIS 5e		TL	175 ± 20	1.12–1.60	5
26	15.657	38.081	MIS 5e	116 ± 13	SB, TL, AM	129 ± 20	0.77–1.22	5
27	15.644	38.065	MIS 5e	116 ± 12	SB, TL, AM	140 ± 20	0.85–1.31	5
28	15.658	38.018	MIS 5e		SB, AM	175 ± 20	1.12–1.60	5
29	15.677	37.968				146 ± 20		5
30	16.227	38.297				92 ± 20		5
31	16.520	38.690				104 ± 20		5
32	17.095	38.893	Holocene	2.99 ± 0.05	RC	0.6		1
33	17.111	39.056	MIS 5e	123	SB, U/Th, AM	100 ± 20	0.55–0.98	5
34(a)	17.111	39.096	MIS 5e	142 ± 20	SB, SF, TL	83 ± 20	0.42–0.83	5
34(b)	17.111	39.096	MIS 5e	149 ± 64	SB, SF, TL	83 ± 20	0.42–0.83	5
35	16.793	39.574				130 ± 20		5
36	16.636	39.583				140 ± 20		5
37	16.396	39.681				135 ± 20		5
38	16.396	39.808				145 ± 20		5
39	16.550	39.897	MIS 5e		AM	142 ± 20	0.87–1.33	3,4,5

199 of a series of en echelon normal faults, whose connecting relay ramps have since been breached  
 200 (e.g. Fossen & Rotevatn, 2016). This model of fault growth is supported by the pres-  
 201 ence of knickpoints along tributaries of the Petrace river, which have been interpreted  
 202 as the geomorphic expression of increases in throw rate (Pirrotta et al., 2016; Roda-Boluda  
 203 & Whittaker, 2017). Further north, the Serre fault has a similar en echelon morphology  
 204 and a length of 35 km (e.g. Galli et al., 2008). Along with the Armo fault in the south,  
 205 they form a linked fault array (Roda-Boluda & Whittaker, 2017), which was probably  
 206 responsible for the  $6.74 \leq M \leq 7.1$  earthquake sequence in 1783 (Galli & Bosi, 2002).

207 Published estimates of average throw rate since the onset of faulting for the Cit-  
 208 tanova fault lie in the range  $0.4 \text{ mm yr}^{-1}$  to  $1.4^{+0.7}_{-0.5} \text{ mm yr}^{-1}$  (Westaway, 1993; Roda-  
 209 Boluda & Whittaker, 2017). Throw rate estimates are similar for the Serre fault, rang-  
 210 ing from  $0.6\text{--}0.7 \text{ mm yr}^{-1}$  (Catalano et al., 2008) to  $0.8^{+0.3}_{-0.2} \text{ mm yr}^{-1}$  (Roda-Boluda &  
 211 Whittaker, 2017). These calculations are based upon an assumed age of the oldest off-  
 212 set marine terrace (Section 1.2.1).

213 The smaller Scilla, Santa Eufemia and Reggio Calabria faults lie close to the Messina  
 214 Strait in the south west of the region, creating a half-graben that is clearly expressed in  
 215 the topography of the Aspromonte area (Figure 2b). Synchronous terrace correlation shows  
 216 that the Vibo fault, on the Tyrrhenian coast of central Calabria, has experienced a throw  
 217 rate of  $\sim 1 \text{ mm yr}^{-1}$  since 340 ka (G. P. Roberts et al., 2013). In the north of Calabria  
 218 lies the Crati basin, a graben bounded by the West and East Crati faults. Both faults  
 219 strike approximately N–S and their traces can be mapped at the surface for  $\sim 50 \text{ km}$  (Fig-  
 220 ures 1 and 2). Offset horizons in reflection seismic data indicate an average throw rate  
 221 for the East Crati fault of  $\geq 0.9 \text{ mm yr}^{-1}$  since 0.7 Ma (Spina et al., 2011). This esti-  
 222 mate agrees with an average throw rate of  $1.3^{+0.7}_{-0.5} \text{ mm yr}^{-1}$  calculated using geomor-  
 223 phic measurements (Roda-Boluda & Whittaker, 2017). Cosmogenic nuclide catchment  
 224 averaged erosion rates from the footwalls of the Serre-Cittanova-Armo fault array vary  
 225 along strike, and some erosion rates equal—within error—the throw rates estimated by  
 226 geomorphic and geologic analyses (Roda-Boluda et al., 2019). On average, however, catch-  
 227 ment averaged erosion rates are a factor of two smaller than uplift rates; this discrep-  
 228 ancy probably arises because catchments are only partially incised by rivers and may have  
 229 experienced different amounts of landsliding (Roda-Boluda et al., 2019). These spatial  
 230 correlations between erosion rates and throw rates suggest that proxies for surface pro-  
 231 cesses can be used to investigate the timing of active faulting (i.e. we can solve the ‘in-  
 232 verse problem’ of quantifying tectonics from changes in topography).

233 While the geologic throw and time-averaged displacement rates for the largest faults  
 234 have been constrained since fault initiation, changes in throw rate have proved more dif-  
 235 ficult to identify because paleoseismicity can only analyse relatively short timescales com-  
 236 pared to geological or geomorphological data (e.g. Galli et al., 2007; Roda-Boluda & Whit-  
 237 taker, 2017). In this paper, we investigate whether fluvial inversion can help to further  
 238 constrain the temporal history of active faulting in Calabria. In particular, we will fo-  
 239 cus on the East Crati, Serre and Cittanova faults.

## 240 2 Methods

### 241 2.1 Longitudinal profile generation

242 To extract a fluvial drainage network across Calabria, Esri’s steepest descent flow  
 243 routing algorithms (Flow Direction and Flow Length), were applied to the SRTM 1 arc  
 244 second ( $\approx 30 \text{ m}$  spatial resolution) digital elevation model (Tarboton, 1997; Stucky de  
 245 Quay et al., 2017). An upstream drainage area of  $0.32 \text{ km}^2$  is assumed to approximate  
 246 the threshold for fluvial incision, and cells with this upstream area were systematically  
 247 sampled to provide the heads of rivers for this study. This technique results in good spa-  
 248 tial coverage of the fluvial network and does not bias against rivers of a particular length  
 249 or stream order assuming that more rivers are extracted from larger catchments. The  
 250 cumulative number of cells that flow into each catchment (Flow Accumulation) was mul-

251 tripled by cell resolution ( $30 \times 30$  m) to calculate upstream area,  $A$ . The morphology  
 252 of the extracted fluvial drainage network was verified using a combination of aerial pho-  
 253 tography, published maps (e.g. Pirrotta et al., 2016) and field surveying. The result of  
 254 longitudinal profile extraction is shown in Figure 4.

255 Two versions of this river inventory were used for fluvial inverse modeling: The first  
 256 contains a drainage network across the whole of Calabria, as presented in Figure 4. For  
 257 the second inventory, we removed all rivers draining the large Crati Basin, where present  
 258 observations of alluviated channels close to the river mouth suggest that a stream power  
 259 erosion model may be less appropriate. The results of the inverse model from the sec-  
 260 ond river inventory are presented in the Supplementary Information; the differences be-  
 261 tween the two models are quantified and discussed therein, and in section 3.1.

## 262 2.2 Stream power erosion models

Field observations show that many of Calabria’s large rivers flow over bedrock with  
 sparse alluvial cover, particularly in the vicinity of the normal faults in the west of the  
 region (e.g. Roda-Boluda & Whittaker, 2017), which suggests that fluvial erosion can  
 be approximated using a detachment-limited model (e.g. Howard, 1994). Erosion rate  
 in a stream power model is parametrised as a function of channel slope, width and dis-  
 charge (Howard, 1994). Upstream area,  $A$ —measured from digital elevation models—  
 is a useful surrogate for discharge and channel width, which are difficult to quantify over  
 geological timescales. Assuming the rate of elevation change,  $\partial z/\partial t$ , is the sum of up-  
 lift rate,  $U$ , and erosion rate,  $E$ , a simple version of the stream power model can be ex-  
 pressed as

$$\frac{\partial z}{\partial t} = U(x, t) + E(x, t), \quad \text{where} \quad E = -KA^m \left( \frac{\partial z}{\partial x} \right)^n, \quad (2)$$

263 where  $K$  is a constant of proportionality often linked to erodibility of the bedrock  
 264 (e.g. Whipple, 2004; Lague, 2014) and  $\partial z/\partial x$  is the longitudinal channel slope. Expo-  
 265 nents  $m$  and  $n$  are positive and are usually empirically evaluated.

266 The exponent,  $n$ , determines the dependency of erosion rate on channel gradient  
 267 and in theory controls the rate of landscape response to perturbation. If  $n$  is not equal  
 268 to 1, the record of tectonic signals can be lost through the formation of shocks and dis-  
 269 continuities (e.g. Pritchard et al., 2009; Royden & Perron, 2013; Lague, 2014; Harel et  
 270 al., 2016). While theoretical considerations may predict that  $n > 1$ —if erosion is con-  
 271 trolled by thresholds associated with stochastic weather events for instance (e.g. Lague,  
 272 2014)—numerous field-based studies of rivers crossing active faults in the central Apen-  
 273 nines and southern Italy have suggested that  $n \sim 1$  is reasonable in this setting. For in-  
 274 stance, the magnitudes and distributions of unit stream power scale predictably with struc-  
 275 tural and geomorphic measures of footwall uplift and fault throw rate for rivers cross-  
 276 ing faults in the Central Apennines of Italy, consistent with  $n = 1$  (Whittaker et al., 2007),  
 277 while a compilation of catchments crossing active faults in Calabria show that normalised  
 278 channel steepness index scales linearly with catchment throw rates, with no distinct litho-  
 279 logical control (c.f. Roda-Boluda & Whittaker, 2017; Roda-Boluda et al., 2019) An anal-  
 280 ysis of knickpoint retreat rates for Italian channels, when hydraulic width scaling is in-  
 281 cluded, also indicates that  $n = 1$  is plausible (Whittaker & Boulton, 2012). Similarly,  
 282 joint-inversion of drainage networks for uplift rate produced low misfits when  $n \approx 1$   
 283 (e.g. Paul et al., 2014; Rudge et al., 2015; McNab et al., 2018), and a unit stream power  
 284 model was derived from longitudinal profile morphology of rivers in central Sardinia (Quye-  
 285 Sawyer et al., 2020). If  $n \approx 1$ , there is a simple, physical relationship between erosion  
 286 process and channel slope (e.g. Whipple & Tucker, 1999), and the stream power model  
 287 can therefore be solved using a computationally efficient linearised inversion approach  
 288 (Goren et al., 2014; Rudge et al., 2015; Glotzbach, 2015). Consequently, we proceed with  
 289  $n = 1$ , though we acknowledge that the value of this exponent remains contentious, and  
 290 we therefore return to this assumption in the discussion.

291 An increase in uplift rate can produce changes in the slope,  $\partial z/\partial x$ , of longitudi-  
 292 nal river profiles known as knickpoints and knickzones. However, an important consid-  
 293 eration when interpreting the shape of longitudinal river profiles is the contribution from  
 294 changes in bedrock competence and discharge. Tensile and compressive rock strength  
 295 is often used a proxy for bedrock erodibility as a function of lithology (e.g. Sklar & Di-  
 296 etrich, 1998; G. G. Roberts & White, 2010; Zondervan et al., 2020). In Calabria, the com-  
 297 pressive strength of bedrock along river channels has been recently measured using a Schmidt  
 298 hammer by Roda-Boluda et al. (2018). These authors found that median Schmidt ham-  
 299 mer rebound values were generally low,  $<35$ , suggesting that bedrock is weak across a  
 300 range of lithologies. These observations indicate that lithology probably does not deter-  
 301 mine the position of Calabria’s knickpoints, therefore we may make the simplifying as-  
 302 sumption that  $K$  is a constant. In addition, if knickpoints are generated by differences  
 303 in rock strength, we may expect knickpoints to systematically correlate with the posi-  
 304 tion of lithologic transitions (e.g. Wobus et al., 2006). Therefore, we will compare the  
 305 location of channel slope discontinuities with mapped bedrock geology to evaluate the  
 306 assumption that changes in lithology do not control the shape of longitudinal profiles.

307 It is possible for fluvial drainage networks to be modified during glacial periods.  
 308 A few glacial deposits have been mapped on the highest peaks in the Pollino range, on  
 309 Mt Sila and in northeastern Calabria (Palmentola et al., 1990). However, since termi-  
 310 nal moraines are found  $>1400$  m above sea-level, and are distributed in an area that lies  
 311 upstream of the threshold for fluvial incision, we conclude that Pleistocene glaciation had  
 312 a negligible effect on Calabria’s fluvial drainage network (Palmentola et al., 1990).

313 Mean annual precipitation measured across Calabria indicates that present-day cou-  
 314 pling between elevation and precipitation is very weak (D’Arcy & Whittaker, 2014). More-  
 315 over, as Calabria has been rapidly uplifted from sea-level during the last  $\sim 1$ Myr, it is  
 316 unlikely that Pleistocene orographic precipitation was more significant than at present  
 317 (section 1.2.1). Paleoclimate reconstructions suggest rainfall in Southern Europe did not  
 318 greatly differ between glacial and interglacial periods (Braconnot et al., 2007). There-  
 319 fore, climatic changes are unlikely to drive long time period differences in fluvial erosion  
 320 rate across Calabria, and we will assume that discharge, which controls erosion rate in  
 321 the stream power model through upstream area,  $A$ , does not vary through time to avoid  
 322 unconstrained model inputs.

323 The major drainage divide passes through the high relief massifs in central Cal-  
 324 abria (Figures 2 and 4), implying that large scale drainage reorganisation has not oc-  
 325 curred since uplift initiated at  $\sim 1$  Ma. Consequently, we suggest that the majority of  
 326 observed knickpoints are unlikely to have been generated by drainage divide migration  
 327 (cf. Willett et al., 2014). Instead, the high number of knickpoints and knickzones across  
 328 the region, many of which are far from the major drainage divide or upstream of active  
 329 faults, suggest that fluvial channels are responding to rock uplift at a variety of spatial  
 330 and temporal scales.

### 331 2.3 Fluvial inverse modeling

332 We used the joint spatial and temporal fluvial inversion model of Rudge et al. (2015)  
 333 to predict the cumulative uplift of Calabria since the exposure of the oldest marine ter-  
 334 race at 0.8–1.2 Ma (section 1.2.1). The advantages of using this type of inverse model  
 335 include the ability to simultaneously analyse large numbers of river profiles and to cal-  
 336 culate uplift rates without the need to pick or classify knickpoints. Moreover, the details  
 337 of fault location, activity and linkage history do not need to be established in advance.

338 The inverse model solves for the spatial distribution of uplift rate on a regular tri-  
 339 angular grid that was generated from evenly spaced vertices 10 km apart. A 10 km ver-  
 340 tex spacing ensures that at least part of a river exists within the vast majority of grid  
 341 cells, so the inverse model should be able to resolve recent uplift rates for most of Cal-  
 342 abria. This vertex spacing is generally less than the fault separation (Figure 3), and is  
 343 much smaller than the area believed to be influenced by regional uplift (Section 1.2), there-

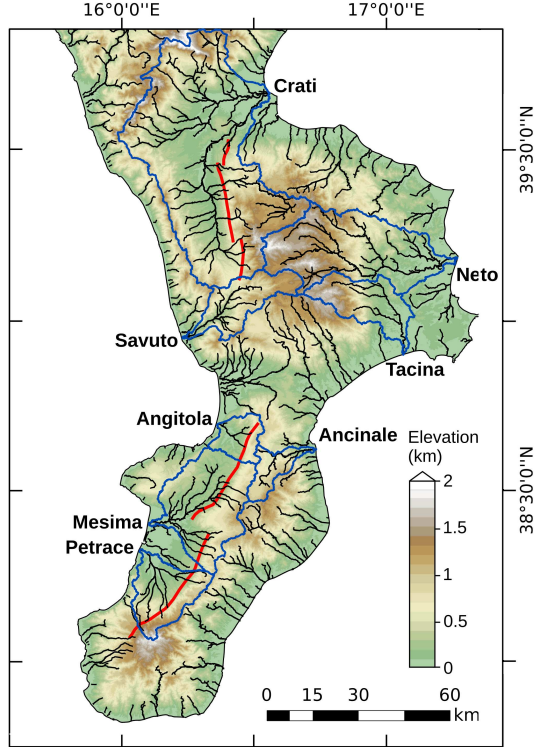


**Figure 4.** Plan view of extracted river profiles overlain on SRTM DEM. Drainage divides of major river basins as blue lines. East Crati, Serre and Cittanova fault traces denoted by red lines (see Figure 2).

344 fore our inverse model may capture uplift caused by both the faulting and regional up-  
 345 lift processes that are known to modify Calabria’s landscape. By modeling uplift on an  
 346 arbitrary grid (i.e. without specifying fault position a priori) we can investigate if the  
 347 inverse model replicates expected geologic behaviour such as divergence in uplift rate be-  
 348 tween the footwall and hanging wall of a mapped fault. Spatial variation in uplift rate  
 349 was linearly interpolated between vertices using barycentric co-ordinates. Predicted up-  
 350 lift rate was permitted to vary at 30 evenly distributed time steps.

351 From Equation 2, the time,  $\tau$ , for a knickpoint to travel between longitudinal dis-  
 352 tances  $x_0$  and  $x_1$  can be written as

$$\tau = \int_{x_0}^{x_1} \frac{1}{KA(x)^m} dx, \quad (3)$$

353 where  $K$  is a proxy for bedrock erodibility and  $A(x)^m$  defines how erosion depends  
 354 on upstream catchment area,  $A$ . Therefore, the predicted elevation,  $z_t$ , of a river chan-  
 355 nel as a function of distance,  $x$ , can be calculated using

$$z_t = \int_0^\tau U(x(t), t) dt, \quad (4)$$

356 where  $U(x(t), t)$  is uplift rate as a function of space and time, which is integrated  
 357 along the time–longitudinal distance path of Equation 3 to derive elevation. For the meth-  
 358 ods employed in this analysis, Equations 3 and 4 were evaluated using the trapezium rule

in order to find the uplift history that produced the observed longitudinal profiles (Rudge et al., 2015).

Equations 3 and 4 show that the stream power incision model (Equation 2) can be linearised such that,  $\mathbf{z} = \mathbf{M}\mathbf{U}$ , where elevation and uplift values are denoted by the vectors  $\mathbf{z}$  and  $\mathbf{U}$ , respectively. This problem tends to be under-determined (i.e. there are more possible uplift models than can be constrained by fluvial profile observations alone), so the inversion model minimises

$$|\mathbf{M}\mathbf{U} - \mathbf{z}|^2 + \lambda_s^2 \int_s \int_{t=0}^{t_{max}} |\nabla U|^2 dt ds \quad \text{subject to: } U \geq 0, \quad (5)$$

where the value of  $\lambda_s$  determines damping in space,  $s$ . Time at the present-day is denoted by  $t = 0$ , and  $t_{max}$  is the maximum possible  $\tau$  for all rivers assuming that a knickpoint can travel from the river mouth to the river head (Rudge et al., 2015). Note that knickpoints can be generated at any position along the river profile using this inverse scheme. Equation 5 was minimised using the non-negative least squares Broyden-Fletcher-Goldfarb-Shanno algorithm of Zhu et al. (1997). The initial uplift rate guess for least-squares minimisation is  $U = 0$  at all nodes in space and time. A positive uplift rate as a function of space and time was incorporated at subsequent iterations if required to produce a better fit between observed and predicted longitudinal profiles. We assume that Equation 5 is minimised when its value differs by  $<10^{-6}$  for consecutive iterations. The uplift rate as a function of space and time that minimises Equation 5 is henceforth known as the best-fitting uplift model.

We followed Parker (1977)'s protocol to seek the smoothest model with the lowest root-mean-squared (rms) misfit, which we will evaluate using independent geologic constraints. In general, inverse models that are highly damped (e.g.  $\lambda_s \gg 1$ ) produce smooth uplift with large rms misfit. A very smooth model (large 'model norm') might not incorporate short wavelength changes in uplift related to normal faulting, and as such would be unsuitable for Calabria. However, models with little damping (e.g.  $\lambda_s \ll 1$ ) can over-fit the data and may be fitting noise (e.g. Parker, 1977). We performed a systematic test of model damping, in which  $\lambda_s$  was varied between  $10^{-3}$  and  $10^3$ , to find an appropriate value of  $\lambda_s$  for this model, and we subsequently evaluate the influence of spatial damping on apparent fault timing (see section 3.2 and Supplementary information).

We calculated the root-mean-squared (rms) misfit to evaluate the extent to which river profiles predicted by the best-fitting uplift model correspond to the observed longitudinal profiles. The rms misfit,  $H$ , was calculated using

$$H = \sqrt{\frac{1}{N} \sum_{i=1}^N \left( \frac{z_{i,o} - z_{i,t}}{\sigma_i} \right)^2}, \quad (6)$$

where  $N$  is the total number of elevation measurements,  $\sigma$  is the error in the observed data, and  $z_o$  and  $z_t$  are elevations of observed and predicted longitudinal river profiles, respectively. The absolute vertical error of SRTM 1 arc second data in high relief regions is  $\approx 16$  m (e.g. Mukul et al., 2017), so we set  $\sigma$  to 16 m.

Inverse approaches can systematically test how the exponent of upstream area,  $m$ , affects rms misfit and calculated uplift. Most published values of  $m$  lie between 0.2–1.0, and  $m = 0.5$  is commonly reported for fluvial settings (e.g. Howard & Kerby, 1983; Bishop et al., 2005; Loget & Van Den Driessche, 2009; Quye-Sawyer et al., 2020). Therefore, we repeated the inversion procedure with values of  $m$  between 0.1 and 1.0 and assumed that suitable average  $m$  values will produce low rms misfits. We also used the inversion modeling to evaluate the average value of bedrock erodibility,  $K$ , for Calabria given the time constraints on the age of the upper terrace (approximately 0.8–1.2 Ma, see section 1.2.1).

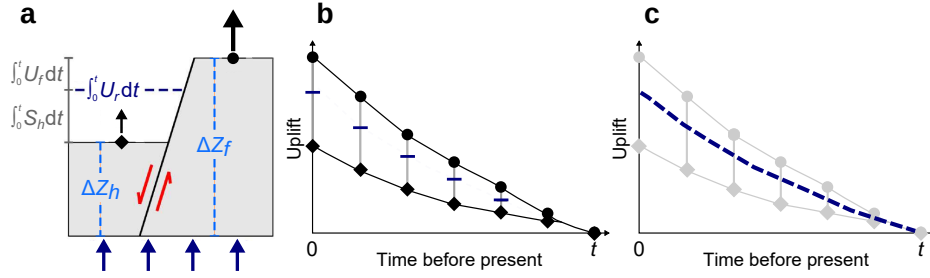


**Figure 5.** Graphical representation of procedure to deconvolve regional uplift from results of fluvial inverse modeling. (a) Fault cross section showing the relative observed uplift,  $\Delta Z_f$ , in fault footwall (circles) and  $\Delta Z_h$  in fault hanging wall (diamonds) for constant regional uplift (blue arrows).  $U_f$  and  $S_h$  indicate magnitudes of footwall uplift rate and hanging wall subsidence rate, respectively. Dashed dark blue line represents the magnitude of regional uplift,  $U_r$ , between time  $t$  and the present day  $t = 0$ . (b) Uplift as a function of time in the footwall and hanging wall (circles and diamonds respectively) with calculated regional uplift denoted by blue dashes. (c) As (b) but with regional uplift linearly interpolated between time  $t$  and the present day.

404 To test the accuracy of our uplift model, we compared uplift rates relative to present  
 405 day sea-level calculated from marine terrace heights to those predicted by inverse mod-  
 406 eling since interglacials MIS 5 and MIS 7. This comparison was restricted to marine ter-  
 407 races with absolute dating constraints, though the analysis still incorporates localities  
 408 across the region, including the minimum and maximum uplift rates since the last in-  
 409 terglacial highstand. For terraces  $>2$  km away from a model vertex, the cumulative up-  
 410 lift map was linearly interpolated so terrace uplift rate and inverse model uplift rate were  
 411 compared at the same spatial location. As geologic and geomorphic evidence suggests  
 412 most of Calabria was a submarine environment prior to early Pleistocene time (section  
 413 1.2.1), and to facilitate comparison between the uplift rates predicted by fluvial inver-  
 414 sion and marine terrace elevations, we have opted to use sea-level as the most appropri-  
 415 ate river base level in this study.

#### 416 2.4 Deconvolution of normal faulting and regional uplift

417 Calabria is experiencing simultaneous regional uplift and extensional faulting, which  
 418 has resulted in some fault hanging walls being uplifted relative to sea-level (Figure 2).  
 419 To deconvolve regional uplift and normal faulting, we first extracted cumulative uplift  
 420 from the best-fitting inverse model at locations in the footwalls and hanging walls of mapped  
 421 faults to estimate long-term throw rates. We subsequently used ratios of footwall uplift  
 422 to hanging wall subsidence to estimate regional uplift through time at the same location.

423 If the oldest terrace (Sicilian Stage, 0.8–1.2 Ma) can be correlated across the tip  
 424 of a fault, being observed in both the footwall and proximal hanging wall, we can calcu-  
 425 late regional uplift using

$$\Delta Z_h = \int_t^T U_r dt - \int_t^T S_h dt, \quad (7)$$

$$\Delta Z_f = \int_t^T U_r dt + \int_t^T U_f dt, \quad (8)$$

$$\int_t^T S_h dt = \alpha \int_t^T U_f dt, \quad (9)$$

where  $\Delta Z_h$  and  $\Delta Z_f$  are changes in the elevation of hanging wall and footwall, respectively.  $U_r$ ,  $S_h$  and  $U_f$  are the rates of regional uplift, hanging wall subsidence and footwall uplift between times  $t$  and  $T$  (Figure 5a).  $\alpha$  is the ratio of hanging wall subsidence to footwall uplift. Substituting Equations 8 and 9 into Equation 7, and rearranging, yields cumulative regional uplift, such that

$$\int_t^T U_r dt = \frac{\Delta Z_h + \alpha \Delta Z_f}{(\alpha + 1)}. \quad (10)$$

Equation 10 can be applied to the inverse model output at every time step to estimate regional uplift through time (Figure 5b,c).

### 3 Results and discussion

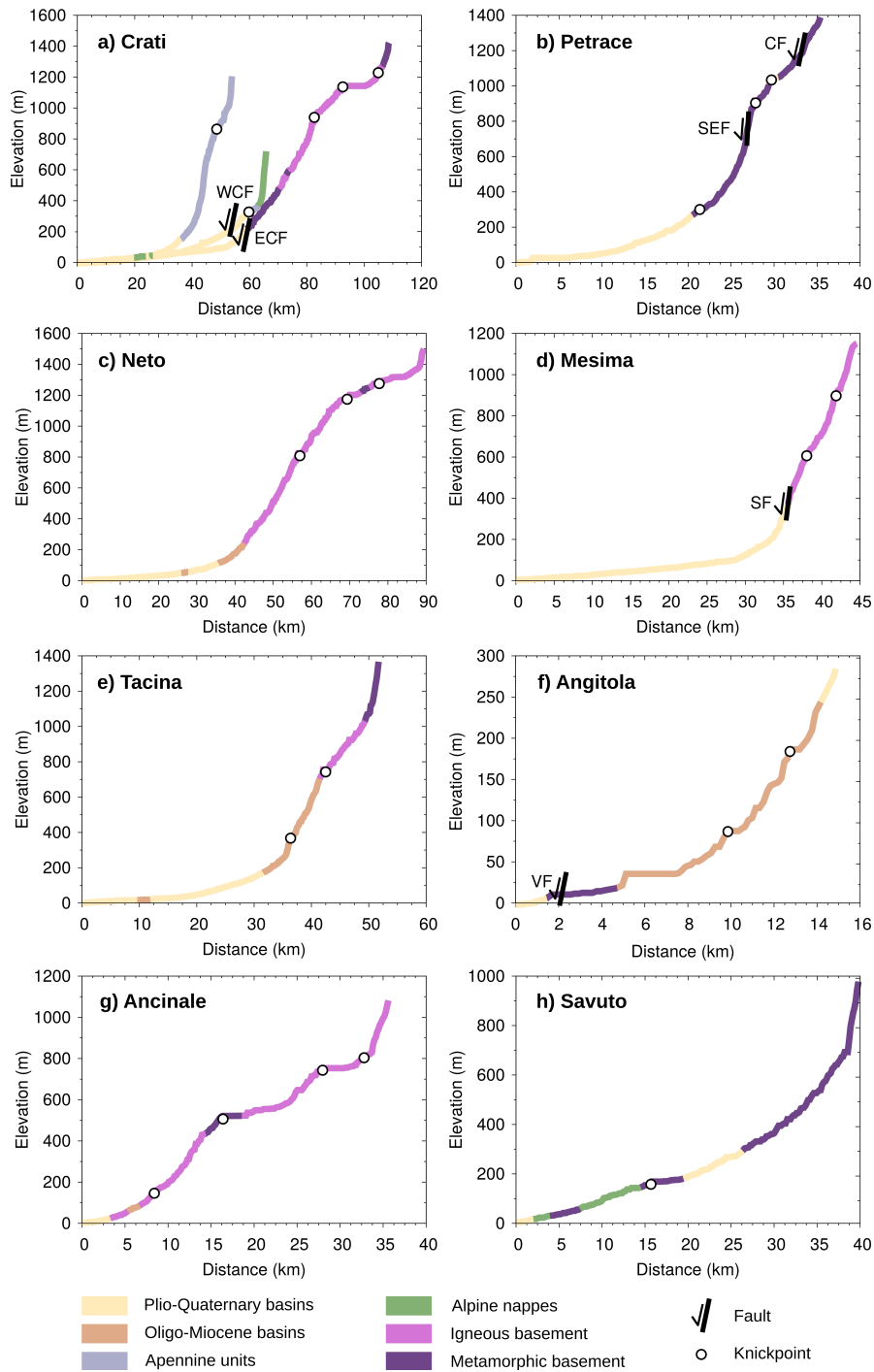
The majority of Calabria’s rivers contain at least one knickpoint or knickzone between  $\approx 100$ – $1200$  m above sea-level (Figures 6 and 7). Although some breaks in channel slope occur on the boundary between different lithologies, such as the knickpoint at 42 m upstream on the Tacina river, knickpoints are not always present on the boundary between these rock types—no knickpoint is present on the boundary between the Oligo-Miocene basins and the igneous basement on the Neto river, for example (Figure 6). In contrast, most knickpoints reside within a single litho-tectonic unit and many are observed upstream of normal faults (Figure 6a,b,d,f). These observations suggest that Calabria’s rivers record uplift that varies in both space and time, and changes in channel slope are not primarily driven by variable bedrock erodibility, in agreement with existing studies at a smaller scale (Glottzbach, 2015; Roda-Boluda & Whittaker, 2017).

For the inverse model, a value of  $\lambda_s \approx 1$  produces a combination of suitable model roughness (a small ‘model norm’) and low rms misfit for Calabria (Figure 8a), which is similar to the optimal value used in many previous studies (e.g. Rudge et al., 2015; G. G. Roberts et al., 2018; Conway-Jones et al., 2019). Therefore, our uplift analysis will initially consider inverse models with  $\lambda_s = 1$ . We will subsequently test the influence of the  $\lambda_s$  value on the apparent fault timing and throw rates inferred from the fluvial inverse model.

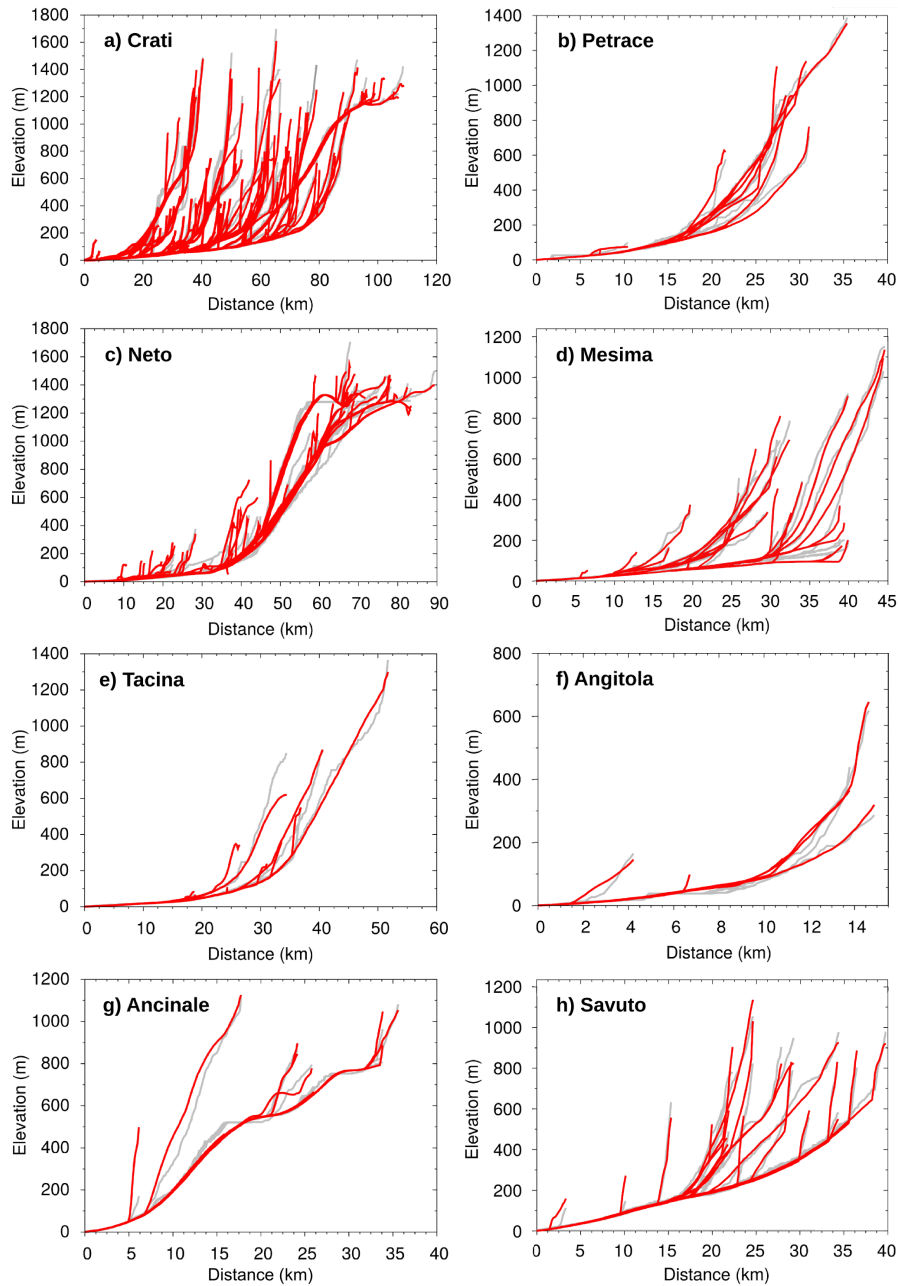
For  $\lambda_s = 1$ , the inverse model fits the data poorly if  $m \lesssim 0.3$  or  $m \gtrsim 0.75$ , which is consistent with previous inversion studies (Figure 8b; e.g. G. G. Roberts et al., 2012). To further constrain the value of  $m$ , we compared the elevation of Capo Vaticano’s highest terrace, with a mean elevation of 550 m above sea-level, to the cumulative uplift calculated from vertices that intersect the terrace (Figure 8c). The highest terrace of Capo Vaticano is one of the most geographically extensive in the region, extending over several vertices in the model mesh, so represents a good location to test the suitability of the inverse model parameters. We aimed to produce models with similar mean elevation to this terrace that also generated theoretical river profiles with a low rms misfit. These results suggest that  $m = 0.65$  is appropriate for fluvial erosion in Calabria (Figure 8b and c).

Figure 7 shows the best-fitting longitudinal profiles of the eight catchments labelled in Figure 4. The rms misfit,  $H$ , is 1.63 for the best-fitting uplift model when  $m = 0.65$  and  $\lambda_s = 1.0$ . Although the  $H$  value is close to unity, implying that—on average—the inverse model almost replicates the observed longitudinal profiles within error, some rivers have better fits than others. Therefore, we calculated the difference between the observed channel elevation and the channel elevation predicted by the inverse model (the ‘elevation residual’,  $z_i^o - z_i^f$ ) as a function of downstream distance for every river. The elevation residuals are normally distributed with a mean of  $-0.04$  m (Figure 9), which suggests that the majority of channel elevations are replicated accurately by the inverse model and elevation is not systematically under- or over-predicted. The standard deviation of the elevation residuals is 26 m, which is the same order of magnitude as the absolute vertical error of the SRTM dataset. The largest elevation residuals ( $\sim 10^2$  m) occur in steep headwaters and across lakes or dams, such as at  $\approx 50$  m upstream on the Neto river (Figures 9 & 7). In general, high residuals are principally a function of model damping, though





**Figure 6.** Longitudinal profiles showing positions of knickpoints and faults in the eight major drainage basins highlighted in Figure 4. (a–h) Trunk streams (and other representative rivers for the Crati catchment) colored according to bedrock geology of Figure 1. WCF: West Crati Fault; ECF: East Crati Fault; CF: Cittanova Fault; SEF: Santa Eufemia Fault; SF: Serre Fault; VF: Vibo Fault. Circles indicate knickpoints identified at abrupt breaks in channel slope not associated with large changes in upstream catchment area.



**Figure 7.** Longitudinal profiles from SRTM data and fluvial inverse modeling. (a–h) Longitudinal profiles extracted from SRTM DEM for the eight catchments highlighted in Figure 4 (plotted as gray lines) and theoretical river profiles (red lines) calculated using uplift history shown in Figure 10.

471 the accuracy of the SRTM data is also likely to decrease in the steep and narrow topog-  
 472 raphy of Calabria’s headwaters (Miliareis & Paraschou, 2005; Mukul et al., 2017).

473 Cumulative uplift for the last twenty model time steps is shown in Figure 10a, and  
 474 uplift rates at each of these time steps are illustrated in Figure 11. We intend to use our  
 475 fluvial inversion model to analyse the uplift that produced the Pleistocene–Recent ma-  
 476 rine terraces, therefore the first time step at which the inversion produces uplift is des-  
 477 ignated an age of 0.8–1.2 Ma (based upon the age of the oldest marine terrace, see sec-

tion 1.2). The age range on the maps in Figures 10a and 11 encompasses the uncertainty in the oldest terrace age at all subsequent time steps. An initial uplift time of 0.8–1.2 Ma corresponds to an average bedrock erodibility  $K = 0.82\text{--}1.22 \text{ m}^{(1-2m)} \text{ Myr}^{-1}$ , noting that an older landscape age would linearly decrease  $K$ , and a younger landscape age would linearly increase  $K$  because bedrock erodibility is directly proportional to erosion rate according to Equation 2.

Model coverage, whose value depends upon the number of channel measurements between mesh vertices as well as stream power parameters  $K$  and  $m$ , decreases at earlier model time steps (Figure 10b). This decrease in model coverage occurs because the wave of fluvial erosion continually migrates upstream through time according to the stream power equation, though an uplift event occurring at a place and time when model coverage is  $>0$  should still be recorded on river profiles today (Figure 10b). Some knickpoints may have reached the river head between the start of uplift and the present day, so uplift events that produced those knickpoints would not be resolved by the inverse model. Nonetheless, model coverage is  $>0$  over most of Calabria during the last  $\sim 700$  ka, which implies that an uplift history can be produced for most of the region at the majority of time steps.

Predicted cumulative uplift from inverse modeling first exceeds 1 km magnitude in the north of Calabria (at  $\sim 300$  ka), then in the Aspromonte region (Figure 10). Uplift of the Serre and Sila Massifs is calculated to occur from 550 ka in the model with initial uplift at 1 Ma, with  $\approx 1$  km of uplift prior to 100 ka in the Serre area. A similar pattern of uplift is predicted from the model for the Sila Massif. More than 500 m of cumulative uplift is observed on the Capo Vaticano peninsula by 72–108 ka, and uplift on the east coast of Calabria is typically less than 500 m throughout the model run. In the hanging wall of the Cittanova fault, and the Crati and Crotone basins, cumulative uplift does not exceed 300 m. Calculated uplift on the footwalls of the Serre and Cittanova faults is initially localised close to the centre of modern day fault traces (see 217 / 325 ka map in Figure 10). Significant cumulative footwall uplift is then observed along a greater extent of the fault array in subsequent time steps.

### 3.1 Evaluation of fluvial inversion results

Given that we have used a simple stream power based erosion equation to model landscape evolution, are the uplift rates calculated from fluvial inverse modeling comparable to existing uplift rate estimates? The majority of uplift rates calculated from the model replicate, within error, uplift rates derived from Mid–Late Pleistocene terrace heights (Figure 12; Table 1). In Figure 12, a range of modeled uplift rates are presented (e.g.  $1.6\text{--}2.2 \text{ mm yr}^{-1}$  for terrace ID = 10) because these ranges take into account the uncertainty in age of the oldest marine terrace (i.e. 0.8–1.2 Ma), which was used to calibrate erodibility,  $K$ , for the inverse model. The highest modeled uplift rate of  $2.5$  to  $3.3 \text{ mm yr}^{-1}$  since MIS 5e coincides with highest observed uplift rate from a terrace on the Capo Vaticano peninsula (Table 1: ID = 14). The smallest uplift rate from the inversion model occurs at the location of one of the lowest last interglacial terraces, near the town of Crotone (Table 1: ID = 34).

The maximum cumulative uplift from the inverse model is 2077 m (Figure 10: 0 ka panel), situated on a vertex close to the northern drainage divide of the Crati catchment near Monte Pollino (2248 m). Large magnitudes of uplift ( $\sim 1$  km) are also predicted at the Sila, Serre and Aspromonte massifs during the youngest time steps (Figure 10). However, the fluvial inverse model assumes that all topography must be generated between 0.8–1.2 Ma and the present day, while the massifs probably had pre-existing relief of  $\sim 10^2$  metres in the Sicilian stage, in contrast with the majority of Calabria (section 1.2). This may explain the high modeled uplift rates at the massifs since 100 ka. Uplift at the massifs is unlikely to be added at the start of the model because model coverage is very poor in these locations and at these time steps (Figure 10b).

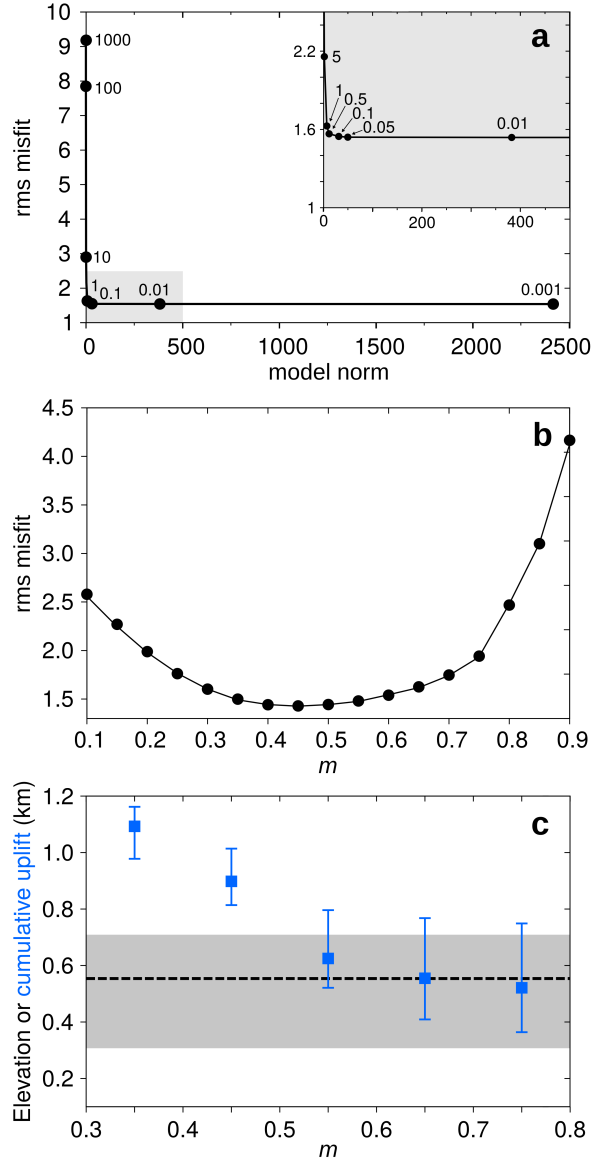


**Figure 8.** (a) Root mean squared (rms) misfit plotted against model norm for  $m = 0.65$ , labelled according to value of  $\lambda_s$ . Grey shaded region enlarged in inset. (b) Root mean squared (rms) misfit as a function of exponent of upstream area,  $m$ , for  $\lambda_s = 1$ . (c) Dashed line: mean elevation; grey polygon: minimum and maximum elevation for the upper terrace on the Capo Vaticano peninsula. Mean (blue squares) and range (blue error bars) of cumulative uplift on the Capo Vaticano peninsula predicted by fluvial inversion at 0 Ma ( $\lambda_s = 1$ ).

530 In addition, we stress that the results presented here are based on the assumption  
 531 that river erosion in Calabria can be approximated by a detachment-limited stream power  
 532 model over the last  $\approx 1$  Myr. This assumption is probably valid for the majority of Cal-  
 533 abria's rivers, especially those in the south of the region that are actively incising across  
 534 several faults with negligible sedimentation in the uplifting hanging walls (Figure 2). How-  
 535 ever, some low lying rivers, such as the those in the large Crati basin, presently contain  
 536 alluvial channels close to the catchment mouth. Although we have few constraints on  
 537 the long-term erosional behaviour of these channels, the assumption of detachment lim-

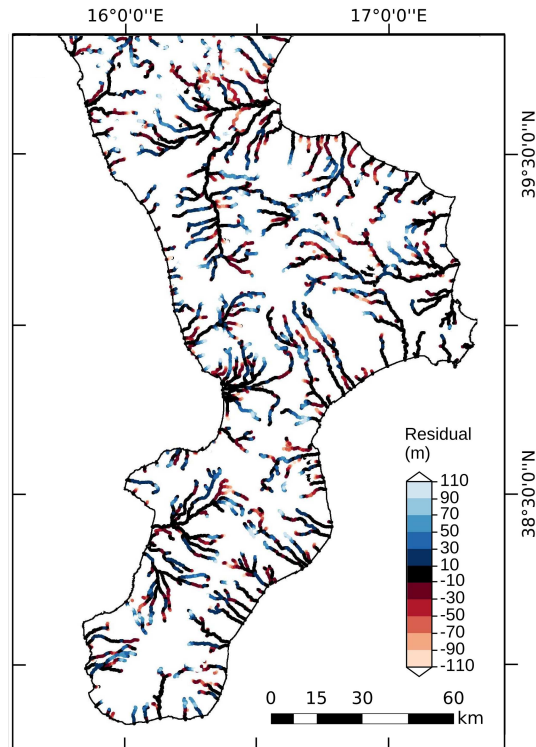


**Figure 9.** Elevation residuals between observed and calculated river longitudinal profiles for best-fitting uplift model.

538 ited erosion may not be appropriate in these areas. Consequently, we removed all rivers  
 539 within the Crati catchment from the inverse model data as a test to investigate the po-  
 540 tential effect of excluding these rivers on our results (Supplementary information and Fig-  
 541 ure S1a, b). However, the difference in predicted uplift between the model containing  
 542 all rivers and the model without the Crati catchment generally does not exceed  $\pm 30$  m  
 543 over a 200 to 300 kyr time interval (Supplementary Figure S1c). The uplift difference  
 544 is usually less than  $\pm 10$  m in the areas containing the Cittanova and Serre faults and  
 545 the dated marine terraces used to compare model and marine terrace uplift rates (Sup-  
 546plementary Figures S1 and S2). Consequently, we conclude that our results are not ma-  
 547terially influenced by the inclusion of the Crati basin in our inverse model (further de-  
 548tails provided in the Supplementary Information).

549 Finally, our analysis also assumes that slope exponent  $n = 1$  in the stream power  
 550 model. While there is ongoing discussion about the value of this exponent in a number  
 551 of settings (e.g. Lague, 2014), we are encouraged that we obtain both a low residual mis-  
 552 fit between the majority of longitudinal profiles and good spatial replication of uplift rate  
 553 patterns denoted by Late Pleistocene marine terraces. We therefore suggest that a detach-  
 554 ment-limited stream power model with  $n = 1$  and  $m = 0.65$  is appropriate to derive a plau-  
 555 sible uplift history for Calabria over the last 1 Myr. We therefore proceed to analyse what  
 556 the inverse model implies about the magnitude of regional uplift and the evolution of  
 557 throw rates for Calabria's faults.

### 558 3.2 Fault throw and regional uplift

559 The results from the inverse model provide an opportunity to analyse the tempo-  
 560 ral evolution of throw rate for the Serre and East Crati faults. The throw of these faults  
 561 can be analysed using fluvial profiles because the thickness of hanging wall sediment is

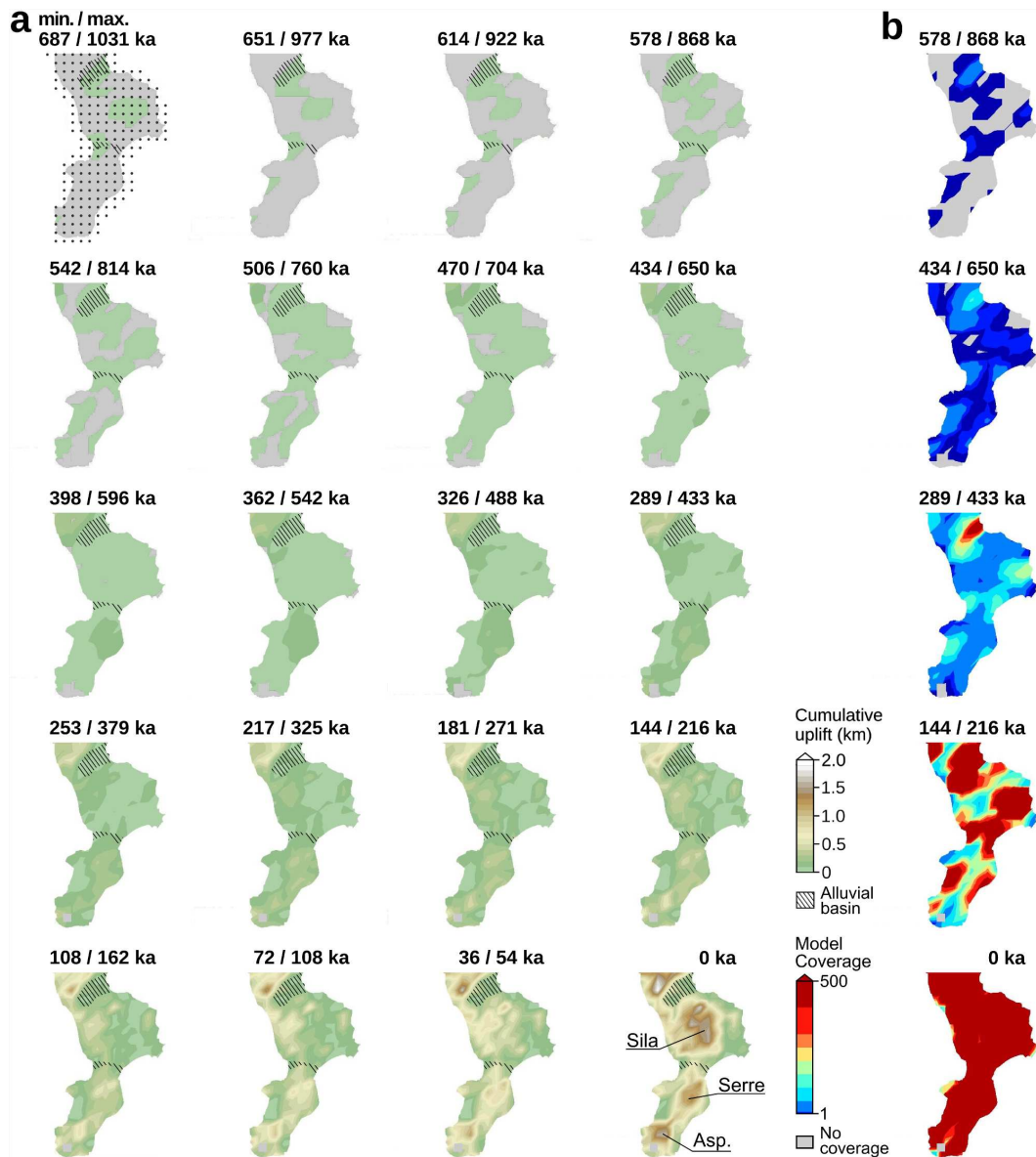


**Figure 10.** Cumulative uplift from best-fitting fluvial inverse model. Age ranges show propagated uncertainty from age of oldest marine terrace. (a) Predicted cumulative uplift maps. Gray circles = inversion model vertices (note 10 km spacing). Uplift rate is interpolated between these vertices along all rivers. Approximate locations of Sila, Serre and Aspromonte (Asp.) massifs indicated on 0 ka map. Hatched regions denote areas where a detachment limited erosional model may not be appropriate, based upon present day observations of alluvial basins. (b) Model coverage.

562 small (Roda-Boluda & Whittaker, 2017), as expected where hanging walls have experi-  
 563 enced significant uplift. For instance, in the Crati basin, reflection seismic and well data  
 564 indicate that Middle Pleistocene to Recent sediment thickness does not exceed 200 m  
 565 (Spina et al., 2011). For hanging wall sediment of negligible thickness, the difference in  
 566 cumulative uplift between footwall and hanging wall approximates fault throw. Cumu-  
 567 lative uplift from the inversion model was extracted from loci 5 km from the Serre and

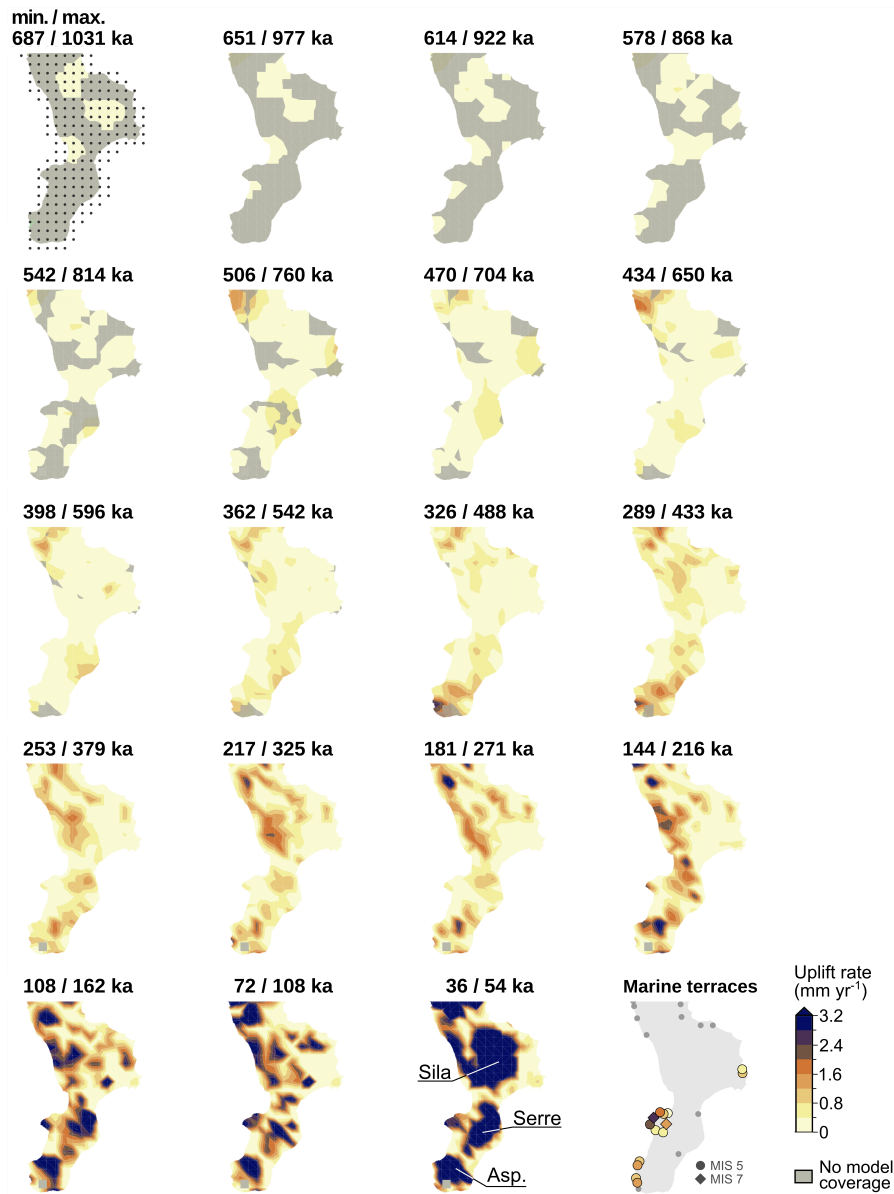


**Figure 11.** Uplift rates producing the best-fitting fluvial inverse model. Gray circles = inversion model vertices at 10 km vertical and horizontal separation. Age ranges show propagated uncertainty from age of oldest marine terrace (minimum age assumes uplift began at 0.8 Ma; maximum age assumes uplift began at 1.2 Ma). Marine terraces map produced using median uplift rates from independent observations in Table 1. Locations of Sila, Serre and Aspromonte (Asp.) massifs indicated on 36 / 54 ka map.

568 East Crati faults, in directions perpendicular to the fault traces, at locations where the  
 569 oldest marine terrace is present in both footwall and hanging wall (Figure 13b and d).  
 570 For the Serre fault, the most extensive footwall terraced area occurs on the southern part  
 571 of the fault, while for the East Crati fault we could extract uplift from the fault centre  
 572 (Figure 13b and d). We interpret the divergence of cumulative uplift at these loci as the  
 573 onset of faulting. We initially discuss the results for  $\lambda_s = 1$  (Figure 13), and results with  
 574 damping parameter  $\lambda_s$  in the range 0.5 to 5 are included in Supplementary Information.

575 Divergence in cumulative uplift indicates that movement on the Serre fault began  
 576 at approximately 650 ka if regional uplift initiates at 1 Ma (770 ka if regional uplift be-  
 577 gins at 1.2 Ma; 510 ka if regional uplift begins at 0.8 Ma), which is 300 ka before move-  
 578 ment on the East Crati fault (Figure 13). This result agrees with asynchronous fault ini-  
 579 tiation estimated from marine terraces offset by faults elsewhere in Calabria (e.g. Zecchin  
 580 et al., 2004). The total amount of throw on the Serre and East Crati faults predicted  
 581 from fluvial inverse modeling (650 m and 800 m, respectively) agrees well with strati-  
 582 graphic observations and measurements of relief (Roda-Boluda & Whittaker, 2017), which  
 583 also gives confidence to our results.

584 We acknowledge that spatial damping of uplift rates in the model, determined by  
 585 the value of  $\lambda_s$ , may affect the estimates of both fault initiation time and total throw  
 586 magnitude. Results where the damping parameter  $\lambda_s$  is varied between 0.5–5.0 are pre-  
 587 sented in Supplementary Figure S3. These results show that reducing  $\lambda_s$  to 0.5 would  
 588 imply fault initiation at 400 Ma for the East Crati Fault and 600 ka for the Serre fault  
 589 (assuming initial uplift at 1 Ma). Apparent throw estimates for the present day are ap-  
 590 proximately 100 m larger than the equivalent interpretation if  $\lambda_s = 1$ , but still lie within  
 591 the range predicted by independent data. Conversely, an increase in  $\lambda_s$  decreases the in-  
 592 ferred age of fault initiation, and  $\lambda_s = 5$  produces an unrealistically small throw mag-  
 593 nitude for the East Crati fault (500 m).

594 Assuming uplift initiates at 1 Ma, and  $\lambda_s = 1$ , average throw rates since the on-  
 595 set of faulting are  $1.1 \text{ mm yr}^{-1}$  for the Serre fault and  $2.3 \text{ mm yr}^{-1}$  for the East Crati  
 596 fault (Figure 13), which are broadly consistent with previous estimates. The modeled  
 597 throw rate on the Serre fault increases markedly at 100 ka ( $\approx 120$  ka if regional uplift be-  
 598 gins at 1.2 Ma;  $\approx 80$  ka if regional uplift begins at 0.8 Ma), which probably records the  
 599 linkage of fault segments as inferred for many fault arrays in the Apennines and elsewhere  
 600 (e.g. Faure Walker et al., 2009; Hopkins & Dawers, 2015). An increase in throw rate is  
 601 also apparent in the  $\lambda_s = 5$  and  $\lambda_s = 0.5$  models (Supplementary Figure S3).

602 The outcome of the inverse model (with uplift initiating at 1 Ma) predicts a grad-  
 603 ual increase in throw rate since  $\sim 0.3$  Ma for the East Crati fault, similar to the calcu-  
 604 lated throw rate for the Serre fault ( $\approx 4 \text{ mm yr}^{-1}$ ) between 120–0 ka. The high throw  
 605 rates predicted by the fluvial inverse model imply that there is a large seismic hazard  
 606 in the region, and the rates are faster than those predicted from fault scarp trenching  
 607 ( $\geq 0.44 \text{ mm yr}^{-1}$ ) for one strand of the Cittanova fault (Galli & Bosi, 2002). While the  
 608 throw rates predicted by these methods are significantly different, they are not neces-  
 609 sarily incompatible with each other. First, the apparent discrepancy between the inverse  
 610 model throw rates and the fault trenching throw rates may arise because of temporal earth-  
 611 quake clustering (fault trenching throw rates are averaged over only 25 ka), spatial vari-  
 612 ation in slip along the fault array—fault trenching rates were obtained near the north  
 613 tip of the Cittanova fault (Galli & Bosi, 2002)—or the assumptions used to estimate the  
 614 initial uplift time in the inverse model. Second, Figure 12 shows that uplift rates pre-  
 615 dicted by the inverse model only replicate uplift rates calculated from marine terrace el-  
 616 evations within a factor of two. When this uncertainty is taken into account, the fault  
 617 throw rates predicted by inverse modeling are consistent with those in the central Apen-  
 618 nines (e.g. Morewood & Roberts, 2000; G. P. Roberts & Michetti, 2004).

619 Catchment averaged erosion rates ( $0.35 \text{ mm yr}^{-1}$  for the southern tip of the Serre  
 620 fault and  $0.32 \text{ mm yr}^{-1}$  for the East Crati fault) are approximately an order of magni-  
 621 tude smaller than our predicted fault throw rates (Roda-Boluda et al., 2019). The large  
 622 difference between the modeled uplift rates and erosion rates partially arises because the  
 623 upstream reaches of many rivers have not reached equilibrium with recent uplift rates,  
 624 so catchment averaged erosion rates may not balance uplift rates across the entire catch-  
 625 ment. The difference between uplift rates and measured erosion rates may also reflect  
 626 the different timescales of investigation. The mean integration time scales of the cosmo-  
 627 genic nuclide erosion rates are 1.7 kyr and 1.9 kyr respectively (Roda-Boluda et al., 2019),  
 628 while the fluvial inverse model only solves for uplift at 36 / 54 kyr time steps (Figures  
 629 10 and 11) so cannot capture rapid fluctuations in erosion rate.



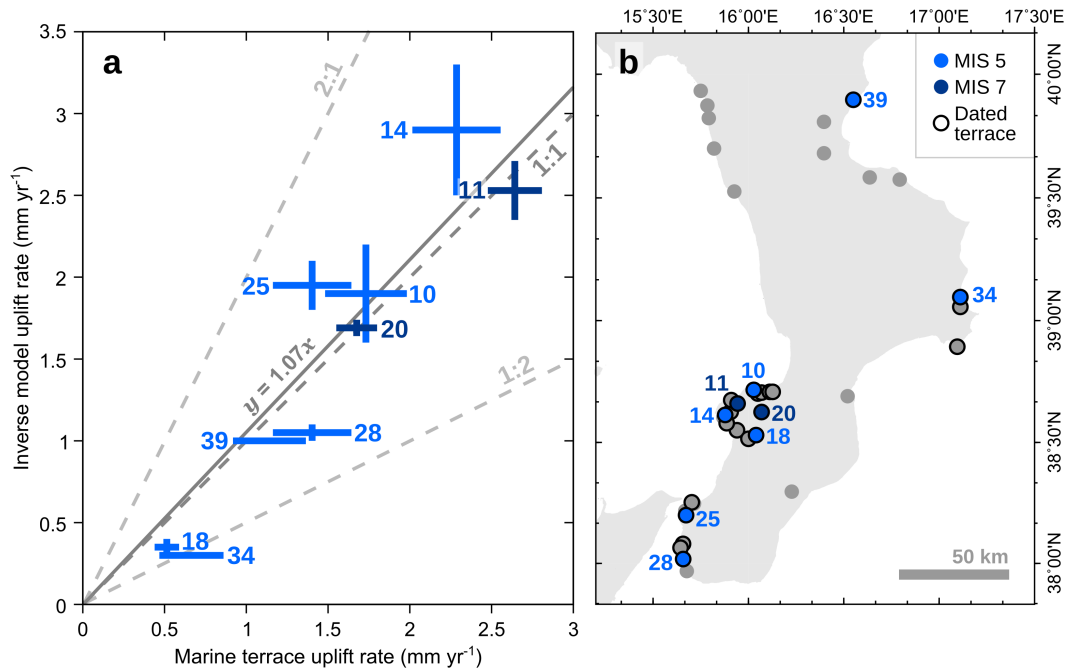


**Figure 12.** MIS 5 and MIS 7 uplift rates from dated terrace elevations and longitudinal profile inverse modeling. (a) Comparison between uplift rates derived from marine terrace elevations and uplift rates derived from fluvial inverse modeling for nine Mid–Late Pleistocene terrace locations. Terrace ID numbers refer to Table 1. Dashed lines denote theoretical 1:1, 2:1 and 1:2 ratios of uplift rates calculated from inverse modeling and marine terraces. Solid line represents linear regression, through the graph origin, between median uplift rates. (b) Map of Mid–Late Pleistocene terraces. Blue circles refer to the locations of MIS 5 and MIS 7 terraces used in this analysis. Locations enclosed in a black circle are all terraces with independent dating constraints (e.g. OSL, biostratigraphic correlation), which includes MIS 3 and Holocene terraces (Table 1).

630 For the Serre fault, similar uplift rates are observed in both the modern footwall  
 631 and hanging wall prior to  $\sim 0.6$  Ma, and the inverse model estimates  $\approx 50$  m of uplift be-  
 632 tween 0.6–1.0 Ma. At the location of the East Crati fault, the inverse model predicts  $\approx 150$  m  
 633 of uplift before faulting begins at  $\sim 0.3$  Ma. These results agree with suggestions of re-  
 634 gional uplift preceding the onset of normal faulting in Calabria.

635 We will now use measured ratios of footwall uplift to hanging wall subsidence to  
 636 calculate regional uplift from  $\sim 1$  Ma to the present day using the methods in section 2.4.  
 637 Terraces are present in both the footwall and proximal hanging wall of the Serre and East  
 638 Crati faults, and the oldest terrace (Sicilian Stage, 0.8–1.2 Ma) can be correlated across  
 639 the tip of the Serre fault, therefore regional uplift can be isolated using Equation 10. For  
 640 Calabria, published estimates of the ratio of hanging wall subsidence to footwall uplift,  
 641  $\alpha$ , lie in the range 1 to 2, with  $\approx 1.6$  calculated from observations on the Armo-Cittanova-  
 642 Serre fault array (Roda-Boluda & Whittaker, 2017).

643 For values of  $\alpha$  within the published range, the total amount of regional uplift cal-  
 644 culated from the inverse model lies between 750 and 900 m, and modeled regional uplift  
 645 rates increase through time for both the Serre and East Crati faults (Figure 13e). The  
 646 best-fitting uplift model estimates the same magnitude of regional uplift for both faults  
 647 from 240 ka to the present. Uncertainties in  $\alpha$  produce small  $< 10^2$  m error bars on es-  
 648 timated regional uplift (Figure 13e, grey shading) so do not greatly affect our interpre-  
 649 tations of regional uplift history.

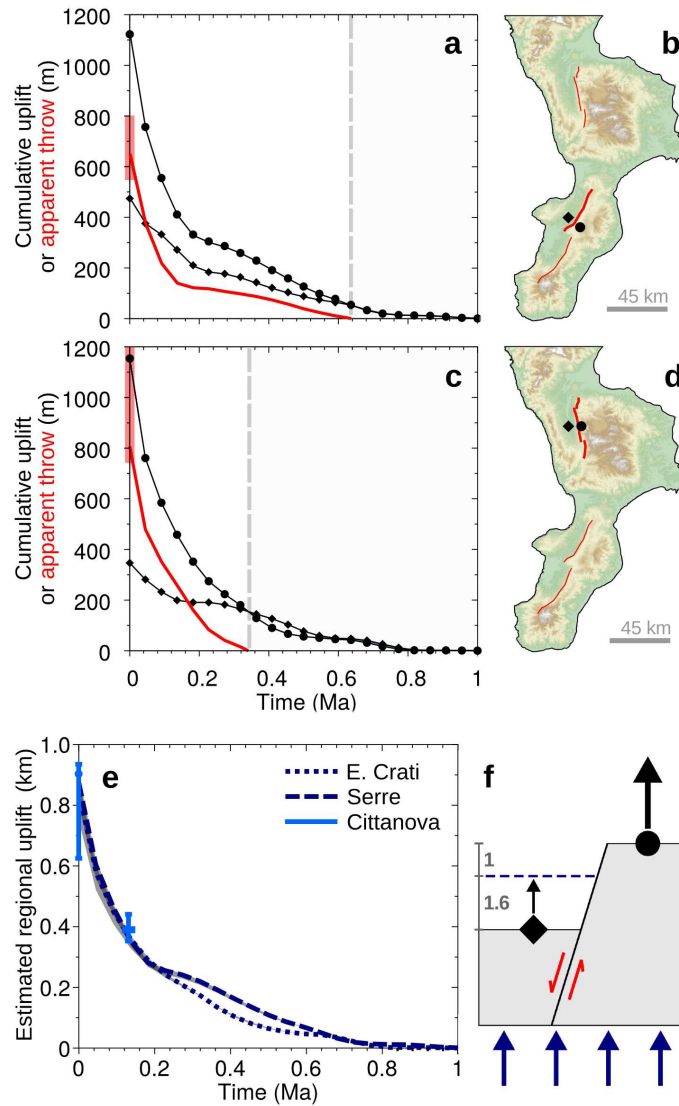


**Figure 13.** Fault-related and regional uplift derived from best-fitting inverse model with initial uplift at 1 Ma. (a) Modeled cumulative uplift of footwall (circles) and hanging wall (diamonds) of the Serre Fault. Red line: Apparent throw (difference in uplift between footwall and hanging wall). Pink line: Geologic estimate of fault throw from Roda-Boluda & Whittaker (2017). Grey dashed line: Onset of fault movement inferred from first separation of model vertices in footwall and hanging wall. (b) Locations of vertices in panel (a). (c–d) Modeled uplift and fault throw for East Crati fault. (e) Calculated regional uplift assuming hanging wall subsidence to footwall uplift ratio  $\alpha = 1.6$  (dashed lines) and  $\alpha$  in the range 1 to 2 (grey shading). Light blue bars: Estimated regional uplift for the Cittanova fault at the present-day and for the last interglacial. (f) Modified version of Figure 5a. Dashed line represents the magnitude of regional uplift without fault movements, assuming  $\alpha = 1.6$ .

650 The oldest terrace offset by the Cittanova fault is well preserved in both the foot-  
 651 wall and in the hanging wall of the Piani d’Aspromonte (Figure 2a,b). Therefore, it is  
 652 possible to estimate the total amount of cumulative uplift solely from terrace observa-  
 653 tions. In this location, footwall elevation is the sum of regional uplift, Cittanova foot-

654 wall uplift and a small amount of vertical motion from the nearby Santa Eufemia and  
 655 Scilla faults. To estimate the magnitude of uplift generated by other faults, we subtracted  
 656 the height of the footwall in the Petrace drainage basin, beyond the northern tip of the  
 657 Santa Eufemia and Scilla faults, from the height of the footwall at Aspromonte (Figure 2b).  
 658 For simplicity, we assume that footwall uplift is similar along strike between these two  
 659 locations (though uplift may have been greatest towards the centre of the footwall). There-  
 660 fore, the magnitude of the regional uplift at the Cittanova fault, for  $\alpha$  between 1 and 2,  
 661 is 620–920 m (Figure 13). Footwall uplift since the last interglacial is extracted from the  
 662 inversion model; hanging wall uplift over the same time period is the height of the ma-  
 663 rine terrace in the Petrace drainage basin (Pirrotta et al., 2016).

664 The similar magnitude and rate of modeled regional uplift indicates that residual  
 665 (i.e. non-fault related) uplift is broadly uniform across central Calabria between the Cit-  
 666 tanova and East Crati faults (Figure 13). Such similarities are unlikely if apparent ob-  
 667 servations of residual regional uplift result from the superposition of footwall uplift from  
 668 multiple large normal faults, and agrees with suggestions of a long-wavelength uplift pro-  
 669 cess operating in the region.

670 A striking feature of our modeled regional uplift is the increase in regional uplift  
 671 rate towards the present day, an increase which has also been suggested from a compar-  
 672 ison of Holocene and MIS 5e marine terrace data (Antonioli et al., 2006). Although up-  
 673 lift models derived from fluvial profile inversion cannot definitively identify the cause of  
 674 landscape change, we can compare the spatial and temporal uplift calculated by the in-  
 675 verse model to uplift patterns predicted by specific geological processes.

676 Long wavelength regional uplift of Calabria has been attributed to processes either  
 677 operating in the sub-lithospheric mantle, lower crustal flow or decoupling of the over-  
 678 riding and subducting plates (e.g. Gvirtzman & Nur, 1999; Wortel & Spakman, 2000;  
 679 Westaway & Bridgland, 2007; Faccenna et al., 2011). For example, Wortel and Spakman  
 680 (2000) propose that a tear in the subducting slab, which has been imaged using p-wave  
 681 tomography beneath southern Italy, could generate long-lived regional uplift due to re-  
 682 bound of the overriding plate. The timing of this slab tear probably coincides with the  
 683 formation of oceanic crust in the Marsili basin between 1.6 and 2.1 Ma (Nicolosi et al.,  
 684 2006; Guillaume et al., 2010), where oceanic spreading is indicative of an increase in stretch-  
 685 ing rate after narrowing of the subducting plate. The results from the inverse model sug-  
 686 gest that regional uplift rates have increased towards the present-day which, assuming  
 687 slab tear is complete, would be inconsistent with decreasing uplift rates predicted dur-  
 688 ing rebound of the lithosphere to reach a new equilibrium elevation (e.g. Buiter et al.,  
 689 2002). However, we cannot rule out a time delay between detachment of the subduct-  
 690 ing slab and uplift of the overriding plate, which appears to depend on the depth of sub-  
 691 duction (Duretz et al., 2011), or an additional, incipient slab tear of smaller magnitude  
 692 that may be inferred from mantle seismicity (Maesano et al., 2017). Therefore, only mul-  
 693 tiple episodes of slab tear, or a time delay between slab tear and rebound, would appear  
 694 to account for the modeled increase in regional uplift rate.

695 However, toroidal mantle flow around the subducting slab beneath Calabria has  
 696 also been inferred from shear wave splitting measurements (Civello & Margheriti, 2004),  
 697 and predicted from seismic tomography, where it correlates well with high topography  
 698 (Faccenna & Becker, 2010). Toroidal flow may generate continued uplift as long as roll-  
 699 back operates, though its rate probably changes through time depending on the trench  
 700 retreat velocity and plate width (Schellart, 2004; Piromallo et al., 2006). Moreover, toroidal  
 701 flow may degrade the lithospheric thermal boundary layer (Zandt & Humphreys, 2008),  
 702 which could produce uplift if the mantle lithosphere is thinned more than the crust (e.g.  
 703 Esedo et al., 2012). While toroidal flow may be responsible for some uplift of the Cal-  
 704 abrian Arc, could toroidal mantle flow account for the temporally increasing uplift rate  
 705 predicted by Figure 13e? Extension of the lithosphere reduces its elastic thickness, which  
 706 may make the overriding plate more susceptible to deformation caused by asthenospheric  
 707 flow (e.g. d’Agostino et al., 2001). Therefore, Calabria may become more easily deformed  
 708 by toroidal mantle flow as faults grow and interact over time, which could result in a tem-

porally increasing regional uplift rate. We hypothesise that if stretching and thinning of the overriding plate has always occurred alongside regional uplift from asthenospheric flow, then the increase in uplift rate predicted by the inverse model could be consistent with ongoing toroidal mantle flow. Results from the inverse model may therefore emphasise the importance of considering geodynamic processes in both lithosphere and asthenosphere, which is often neglected—or difficult to replicate—in numerical or physical models.

## 4 Conclusions

We have utilised a spatial and temporal inversion of river longitudinal profiles to calculate uplift of Calabria, southern Italy. Erosion rates in a stream power model were calibrated using the age of the oldest marine terrace exposed throughout Calabria. Uplift calculated by fluvial inverse modeling is consistent with uplift rates derived from dated last interglacial marine terraces, which indicates that a simple stream power equation can effectively model uplift and erosion in Calabria. Our results are consistent with variable uplift of Calabria since the Early Pleistocene from normal faults and regional processes, predicting 650 m and 800 m of total apparent throw on the Serre and East Crati faults, respectively. Fault throw calculated from fluvial inversion is consistent with independent measurements of structural relief, and increases in throw rate are suggestive of fault interaction and linkage. Fluvial inversion, therefore, is shown to be a useful technique to analyse fault array evolution. Non-fault related (i.e. regional) cumulative uplift superimposed on three of Calabria's major faults is responsible for  $\approx 850$  m of uplift, and regional uplift rates appear to have increased towards the present day. An increase in regional uplift rate may indicate the combined effect of lithospheric weakness and ongoing mantle flow processes.

## Acknowledgments

This work was supported by a studentship from the Natural Environment Research Council (NERC) to JQS. River profiles are available from the National Geoscience Data Centre (<https://dx.doi.org/10.5285/602a0a95-3541-408b-8ded-87d542d558e2>). The authors would like to thank Liran Goren and an anonymous reviewer for their comments that helped improve the manuscript. The authors declare no conflicts of interest for this work.

## References

- Antonioli, F., Ferranti, L., Fontana, A., Amorosi, A., Bondesan, A., Braitenberg, C., ... Stocchi, P. (2009). Holocene relative sea-level changes and vertical movements along the Italian and Istrian coastlines. *Quaternary International*, *206*(1-2), 102-133. doi: 10.1016/j.quaint.2008.11.008
- Antonioli, F., Ferranti, L., Lambeck, K., Kershaw, S., Verrubbi, V., & Dai Pra, G. (2006). Late Pleistocene to Holocene record of changing uplift rates in southern Calabria and northeastern Sicily (southern Italy, Central Mediterranean Sea). *Tectonophysics*, *422*(1), 23-40. doi: 10.1016/j.tecto.2006.05.003
- Baccheschi, P., Margheriti, L., & Steckler, M. S. (2008). SKS splitting in Southern Italy: Anisotropy variations in a fragmented subduction zone. *Tectonophysics*, *462*(14), 49-67. doi: 10.1016/j.tecto.2007.10.014
- Bianca, M., Catalano, S., De Guidi, G., Gueli, A. M., Monaco, C., Ristuccia, G. M., ... Troja, S. O. (2011). Luminescence chronology of Pleistocene marine terraces of Capo Vaticano peninsula (Calabria, Southern Italy). *Quaternary International*, *232*(1-2), 114-121. doi: 10.1016/j.quaint.2010.07.013
- Bishop, P., Hoey, T. B., Jansen, J. D., & Artza, I. L. (2005). Knickpoint recession rate and catchment area: the case of uplifted rivers in Eastern Scotland. *Earth Surface Processes and Landforms*, *30*(6), 767-778. doi: 10.1002/esp.1191

- 758 Boulton, S., Stokes, M., & Mather, A. (2014). Transient fluvial incision as an indi-  
759 cator of active faulting and Plio-Quaternary uplift of the Moroccan High Atlas.  
760 *Tectonophysics*, *633*, 16-33. doi: 10.1016/j.tecto.2014.06.032
- 761 Braconnot, P., Otto-Bliesner, B., Harrison, S., Joussaume, S., Peterchmitt, J.-Y.,  
762 Abe-Ouchi, A., . . . others (2007). Results of PMIP2 coupled simulations of the  
763 Mid-Holocene and Last Glacial Maximum—Part 1: experiments and large-scale  
764 features. *Climate of the Past*, *3*(2), 261-277. doi: 10.5194/cp-3-261-2007
- 765 Braga, J. C., Martín, J. M., & Quesada, C. (2003). Patterns and average rates of  
766 late Neogene-Recent uplift of the Betic Cordillera, SE Spain. *Geomorphology*,  
767 *50*(1), 3-26. doi: 10.1016/S0169-555X(02)00205-2
- 768 Buiter, S. J., Govers, R., & Wortel, M. (2002). Two-dimensional simulations of  
769 surface deformation caused by slab detachment. *Tectonophysics*, *354*(3-4), 195-  
770 210. doi: 10.1016/S0040-1951(02)00336-0
- 771 Capozzi, R., Artoni, A., Torelli, L., Lorenzini, S., Oppo, D., Mussoni, P., & Polonia,  
772 A. (2012). Neogene to Quaternary tectonics and mud diapirism in the Gulf  
773 of Squillace (Crotono-Spartivento Basin, Calabrian Arc, Italy). *Marine and*  
774 *Petroleum Geology*, *35*(1), 219-234. doi: 10.1016/j.marpetgeo.2012.01.007
- 775 Carobene, L., & Dai Pra, G. (1990). Genesis, chronology and tectonics of the Qua-  
776 ternary marine terraces of the Tyrrhenian coast of Northern Calabria (Italy).  
777 Their correlation with climatic variations. *Il Quaternario*, *3*(2), 75-94.
- 778 Catalano, S., De Guidi, G., Monaco, C., Tortorici, G., & Tortorici, L. (2008). Active  
779 faulting and seismicity along the Siculo–Calabrian Rift Zone (Southern Italy).  
780 *Tectonophysics*, *453*(14), 177-192. doi: 10.1016/j.tecto.2007.05.008
- 781 Chiarabba, C., Jovane, L., & DiStefano, R. (2005). A new view of Italian seismic-  
782 ity using 20 years of instrumental recordings. *Tectonophysics*, *395*(3), 251-268.  
783 doi: 10.1016/j.tecto.2004.09.013
- 784 Cinti, F., Alfonsi, L., D’Alessio, A., Marino, S., & Brunori, C. (2015). Fault-  
785 ing and Ancient Earthquakes at Sybaris Archaeological Site, Ionian Cal-  
786 abria, Southern Italy. *Seismological Research Letters*, *86*(1), 245-254. doi:  
787 10.1785/02201401071
- 788 Civello, S., & Margheriti, L. (2004). Toroidal mantle flow around the Calabrian slab  
789 (Italy) from SKS splitting. *Geophysical Research Letters*, *31*(10), L10601. doi:  
790 10.1029/2004GL019607
- 791 Commins, D., Gupta, S., & Cartwright, J. (2005). Deformed streams reveal growth  
792 and linkage of a normal fault array in the Canyonlands graben, Utah. *Geology*,  
793 *33*(8), 645-648. doi: 10.1130/G21433AR.1
- 794 Conway-Jones, B. W., Roberts, G. G., Fichtner, A., & Hoggard, M. (2019). Neogene  
795 epeirogeny of Iberia. *Geochemistry, Geophysics, Geosystems*, *20*(2), 1138-1163.  
796 doi: 10.1029/2018GC007899
- 797 Cowie, P., Gupta, S., & Dawers, N. (2000). Implications of fault array evolution for  
798 synrift depocentre development: insights from a numerical fault growth model.  
799 *Basin Research*, *12*(3-4), 241-261. doi: 10.1111/j.1365-2117.2000.00126.x
- 800 Cowie, P., Phillips, R., Roberts, G., McCaffrey, K., Zijerveld, L., Gregory, L., . . .  
801 Wilkinson, M. (2017). Orogen-scale uplift in the central Italian Apennines  
802 drives episodic behaviour of earthquake faults. *Scientific Reports*, *7*, 44858.  
803 doi: 10.1038/srep44858
- 804 Cucci, L. (2004). Raised marine terraces in the Northern Calabrian Arc (South-  
805 ern Italy): a 600 kyr-long geological record of regional uplift. *Annals of Geo-*  
806 *physics*, *47*(4). doi: 10.4401/ag-3350
- 807 Cucci, L., & Cinti, F. R. (1998). Regional uplift and local tectonic deformation  
808 recorded by the Quaternary marine terraces on the Ionian coast of  
809 northern Calabria (southern Italy). *Tectonophysics*, *292*(1), 67-83. doi:  
810 10.1016/S0040-1951(98)00061-4
- 811 Cyr, A. J., Granger, D. E., Olivetti, V., & Molin, P. (2010). Quantifying rock uplift  
812 rates using channel steepness and cosmogenic nuclide-determined erosion rates:

- 813 Examples from northern and southern Italy. *Lithosphere*, 2(3), 188-198. doi:  
814 10.1130/196.1
- 815 Czarnota, K., Roberts, G., White, N., & Fishwick, S. (2014). Spatial and tem-  
816 poral patterns of Australian dynamic topography from River Profile Model-  
817 ing. *Journal of Geophysical Research: Solid Earth*, 119(2), 1384-1424. doi:  
818 10.1002/2013JB010436
- 819 d'Agostino, N., Jackson, J., Dramis, F., & Funiciello, R. (2001). Interactions be-  
820 tween mantle upwelling, drainage evolution and active normal faulting: an  
821 example from the central Apennines (Italy). *Geophysical Journal Interna-*  
822 *tional*, 147(2), 475-497. doi: 10.1046/j.1365-246X.2001.00539.x
- 823 D'Arcy, M., & Whittaker, A. C. (2014). Geomorphic constraints on landscape sen-  
824 sitivity to climate in tectonically active areas. *Geomorphology*, 204, 366-381.  
825 doi: 10.1016/j.geomorph.2013.08.019
- 826 Duretz, T., Gerya, T. V., & May, D. A. (2011). Numerical modelling of spontaneous  
827 slab breakoff and subsequent topographic response. *Tectonophysics*, 502(1-2),  
828 244-256. doi: 10.1016/j.tecto.2010.05.024
- 829 Esedo, R., van Wijk, J., Coblenz, D., & Meyer, R. (2012). Uplift prior to conti-  
830 nental breakup: Indication for removal of mantle lithosphere? *Geosphere*, 8(5),  
831 1078-1085. doi: 10.1130/GES00748.1
- 832 Faccenna, C., & Becker, T. (2010). Shaping mobile belts by small-scale convection.  
833 *Nature*, 465, 602-605. doi: 10.1038/nature09064
- 834 Faccenna, C., Becker, T. W., Auer, L., Billi, A., Boschi, L., Brun, J. P., ... Jolivet,  
835 L. (2014). Mantle dynamics in the Mediterranean. *Reviews of Geophysics*,  
836 52(3), 283-332. doi: 10.1002/2013RG000444
- 837 Faccenna, C., Molin, P., Orecchio, B., Olivetti, V., Bellier, O., Funiciello, F., ...  
838 Billi, A. (2011). Topography of the Calabria subduction zone (southern  
839 Italy): Clues for the origin of Mt. Etna. *Tectonics*, 30(1), TC1003. doi:  
840 10.1029/2010TC002694
- 841 Faure Walker, J., Roberts, G., Cowie, P., Papanikolaou, I., Sammonds, P., Michetti,  
842 A., & Phillips, R. (2009). Horizontal strain-rates and throw-rates across  
843 breached relay zones, central Italy: Implications for the preservation of throw  
844 deficits at points of normal fault linkage. *Journal of Structural Geology*, 31,  
845 1145-1160. doi: 10.1016/j.jsg.2009.06.011
- 846 Faure Walker, J., Roberts, G. P., Cowie, P., Papanikolaou, I., Michetti, A., Sam-  
847 monds, P., ... Phillips, R. (2012). Relationship between topography,  
848 rates of extension and mantle dynamics in the actively-extending Ital-  
849 ian Apennines. *Earth and Planetary Science Letters*, 325, 76-84. doi:  
850 10.1016/j.epsl.2012.01.028
- 851 Fellin, M. G., Zattin, M., Picotti, V., Reiners, P. W., & Nicolescu, S. (2005). Relief  
852 evolution in northern Corsica (western Mediterranean): Constraints on uplift  
853 and erosion on long-term and short-term timescales. *Journal of Geophysical*  
854 *Research: Earth Surface*, 110(F1), F0016. doi: 10.1029/2004JF000167
- 855 Ferranti, L., Antonioli, F., Mauz, B., Amorosi, A., Dai Pra, G., Mastronuzzi, G., ...  
856 Radtke, U. (2006). Markers of the last interglacial sea-level high stand along  
857 the coast of Italy: tectonic implications. *Quaternary international*, 145, 30-54.  
858 doi: 10.1016/j.quaint.2005.07.009
- 859 Ferranti, L., Oldow, J. S., D'Argenio, B., Catalano, R., Lewis, D., Marsella, E., ...  
860 Pepe, F. (2008). Active deformation in southern Italy, Sicily and southern  
861 Sardinia from GPS velocities of the Peri-Tyrrhenian Geodetic Array (PTGA).  
862 *Bollettino della Società Geologica Italiana*, 127(2), 299-316.
- 863 Fiannacca, P., Cirrincione, R., Bonanno, F., & Carciotto, M. M. (2015). Source-  
864 inherited compositional diversity in granite batholiths: The geochemical mes-  
865 sassage of Late Paleozoic intrusive magmatism in central Calabria (southern  
866 Italy). *Lithos*, 236-237, 123-140. doi: 10.1016/j.lithos.2015.09.003
- 867 Ford, M., Rohais, S., Williams, E. A., Bourlange, S., Jousset, D., Backert,

- 868 N., & Malartre, F. (2013). Tectono-sedimentary evolution of the west-  
 869 ern Corinth rift (Central Greece). *Basin Research*, *25*(1), 3-25. doi:  
 870 10.1111/j.1365-2117.2012.00550.x
- 871 Fossen, H., & Rotevatn, A. (2016). Fault linkage and relay structures in extensional  
 872 settings—A review. *Earth-Science Reviews*, *154*, 14-28. doi: 10.1016/j.earscirev  
 873 .2015.11.014
- 874 Fox, M., Goren, L., May, D. A., & Willett, S. D. (2014). Inversion of fluvial channels  
 875 for paleorock uplift rates in Taiwan. *Journal of Geophysical Research: Earth  
 876 Surface*, *119*(9), 1853-1875. doi: 10.1002/2014JF003196
- 877 Galli, P., & Bosi, V. (2002). Paleoseismology along the Cittanova fault: impli-  
 878 cations for seismotectonics and earthquake recurrence in Calabria (southern  
 879 Italy). *Journal of Geophysical Research: Solid Earth*, *107*(B3), 2044. doi:  
 880 10.1029/2001JB000234
- 881 Galli, P., Galadini, F., & Pantosti, D. (2008). Twenty years of paleoseismology in  
 882 Italy. *Earth-Science Reviews*, *88*(1), 89-117. doi: 10.1016/j.earscirev.2008.01  
 883 .001
- 884 Galli, P., Scionti, V., & Spina, V. (2007). New paleoseismic data from the Lakes and  
 885 Serre faults: seismotectonic implications for Calabria (Southern Italy). *Bollet-  
 886 tino della Società Geologica Italiana*, *126*(2), 347-364.
- 887 Glotzbach, C. (2015). Deriving rock uplift histories from data-driven inversion of  
 888 river profiles. *Geology*, *43*(6), 467-470. doi: 10.1130/G36702.1
- 889 Goren, L., Fox, M., & Willett, S. D. (2014). Tectonics from fluvial topography using  
 890 formal linear inversion: Theory and applications to the Inyo Mountains, Cal-  
 891 ifornia. *Journal of Geophysical Research: Earth Surface*, *119*(8), 1651-1681.  
 892 doi: 10.1002/2014JF003079
- 893 Guillaume, B., Funiciello, F., Faccenna, C., Martinod, J., & Olivetti, V. (2010).  
 894 Spreading pulses of the Tyrrhenian Sea during the narrowing of the Calabrian  
 895 slab. *Geology*, *38*(9), 819-822. doi: 10.1130/G31038.1
- 896 Gvirtzman, Z., & Nur, A. (1999). Plate detachment, asthenosphere upwelling, and  
 897 topography across subduction zones. *Geology*, *27*(6), 563-566. doi: 10.1130/  
 898 0091-7613(1999)027\$(\$0563:PDAUAT\$)\$2.3.CO;2
- 899 Harel, M.-A., Mudd, S., & Attal, M. (2016). Global analysis of the stream power law  
 900 parameters based on worldwide <sup>10</sup>Be denudation rates. *Geomorphology*, *268*,  
 901 184-196. doi: 10.1016/j.geomorph.2016.05.035
- 902 Hopkins, M., & Dawers, N. (2015). Changes in bedrock channel morphology driven  
 903 by displacement rate increase during normal fault interaction and linkage.  
 904 *Basin Research*, *27*, 43-59. doi: 10.1111/bre.12072
- 905 Howard, A. D. (1994). A detachment-limited model of drainage basin evolution.  
 906 *Water resources research*, *30*(7), 2261-2285. doi: 10.1029/94WR00757
- 907 Howard, A. D., & Kerby, G. (1983). Channel changes in badlands. *Geological Society  
 908 of America Bulletin*, *94*, 739-752. doi: 10.1130/0016-7606(1983)94(739:CCIB)2  
 909 .0.CO;2
- 910 Kirby, E., & Whipple, K. (2001). Quantifying differential rock-uplift rates  
 911 via stream profile analysis. *Geology*, *29*(5), 415-418. doi: 10.1130/  
 912 0091-7613(2001)029(0415:qdrurv)2.0.co;2
- 913 Kirby, E., & Whipple, K. X. (2012). Expression of active tectonics in erosional land-  
 914 scapes. *Journal of Structural Geology*, *44*, 54-75. doi: 10.1016/j.jsg.2012.07  
 915 .009
- 916 Lague, D. (2014). The stream power river incision model: evidence, theory and be-  
 917 yond. *Earth Surface Processes and Landforms*, *39*, 38-61. doi: 10.1002/esp  
 918 .3462
- 919 Li, G., West, A. J., Densmore, A. L., Hammond, D. E., Jin, Z., Zhang, F., ...  
 920 Hilton, R. G. (2016). Connectivity of earthquake-triggered landslides with  
 921 the fluvial network: Implications for landslide sediment transport after the  
 922 2008 Wenchuan earthquake. *Journal of Geophysical Research: Earth Surface*,

- 923           121(4), 703-724. doi: 10.1002/2015JF003718
- 924   Liberi, F., Morten, L., & Piluso, E. (2006). Geodynamic significance of ophiolites  
925       within the Calabrian Arc. *Island Arc*, 15(1), 26-43. doi: 10.1111/j.1440-1738  
926       .2006.00520.x
- 927   Loget, N., & Van Den Driessche, J. (2009). Wave train model for knickpoint migra-  
928       tion. *Geomorphology*, 106(34), 376-382. doi: 10.1016/j.geomorph.2008.10.017
- 929   Longhitano, S. G. (2011). The record of tidal cycles in mixed silici-bioclastic  
930       deposits: examples from small Plio-Pleistocene peripheral basins of the mi-  
931       crotidal Central Mediterranean Sea. *Sedimentology*, 58(3), 691-719. doi:  
932       10.1111/j.1365-3091.2010.01179.x
- 933   Longhitano, S. G., Chiarella, D., Di Stefano, A., Messina, C., Sabato, L., & Tro-  
934       peano, M. (2012). Tidal signatures in Neogene to Quaternary mixed deposits  
935       of southern Italy straits and bays. *Sedimentary Geology*, 279, 74-96. doi:  
936       10.1016/j.sedgeo.2011.04.019
- 937   Maesano, F. E., Tiberti, M. M., & Basili, R. (2017). The Calabrian Arc: three-  
938       dimensional modelling of the subduction interface. *Scientific Reports*, 7, 8887.  
939       doi: 10.1038/s41598-017-09074-8
- 940   Magni, V., Faccenna, C., van Hunen, J., & Funicello, F. (2014). How collision trig-  
941       gers backarc extension: Insight into Mediterranean style of extension from 3-D  
942       numerical models. *Geology*, 42(6), 511-514. doi: 10.1130/G35446.1
- 943   Malinverno, A., & Ryan, W. B. (1986). Extension in the Tyrrhenian Sea and  
944       shortening in the Apennines as result of arc migration driven by sinking of the  
945       lithosphere. *Tectonics*, 5(2), 227-245. doi: 10.1029/TC005i002p00227
- 946   Marc, O., Hovius, N., & Meunier, P. (2016). The mass balance of earthquakes and  
947       earthquake sequences. *Geophysical Research Letters*, 43(8), 3708-3716. doi: 10  
948       .1002/2016GL068333
- 949   McLeod, A. E., Dawers, N. H., & Underhill, J. R. (2000). The propagation  
950       and linkage of normal faults: insights from the Strathspey-Brent-Statfjord  
951       fault array, northern North Sea. *Basin Research*, 12(3-4), 263-284. doi:  
952       10.1111/j.1365-2117.2000.00124.x
- 953   McNab, F., Ball, P. W., Hoggard, M. J., & White, N. J. (2018). Neogene Uplift  
954       and Magmatism of Anatolia: Insights From Drainage Analysis and Basaltic  
955       Geochemistry. *Geochemistry, Geophysics, Geosystems*, 19(1), 175-213. doi:  
956       10.1002/2017GC007251
- 957   Meschis, M., Roberts, G. P., Mildon, Z., Robertson, J., Michetti, A., &  
958       Faure Walker, J. (2019). Slip on a mapped normal fault for the 28<sup>th</sup> De-  
959       cember 1908 Messina earthquake (Mw 7.1) in Italy. *Scientific reports*, 9(1),  
960       6481. doi: 10.1038/s41598-019-42915-2
- 961   Miliareisis, G., & Paraschou, C. (2005). Vertical accuracy of the SRTM DTED level  
962       1 of Crete. *International Journal of Applied Earth Observation and Geoinfor-  
963       mation*, 7, 49-59. doi: 10.1016/j.jag.2004.12.001
- 964   Minelli, L., & Faccenna, C. (2010). Evolution of the Calabrian accretionary  
965       wedge (central Mediterranean). *Tectonics*, 29(4), TC4004. doi: 10.1029/  
966       2009TC002562
- 967   Mirabella, F., Brozzetti, F., Lupattelli, A., & Barchi, M. R. (2011). Tec-  
968       tonic evolution of a low-angle extensional fault system from restored cross-  
969       sections in the Northern Apennines (Italy). *Tectonics*, 30(6), TC6002. doi:  
970       10.1029/2011TC002890
- 971   Miyachi, T., Dai Pra, G., & Sylos Labini, S. (1994). Geochronology of Pleis-  
972       tocene marine terraces and regional tectonics in the Tyrrhenian coast of South  
973       Calabria, Italy. *Il Quaternario*, 7(1), 17-34.
- 974   Monaco, C., & Tortorici, L. (2000). Active faulting in the Calabrian arc and eastern  
975       Sicily. *Journal of Geodynamics*, 29(3-5), 407-424. doi: 10.1016/S0264-3707(99)  
976       00052-6
- 977   Morewood, N. C., & Roberts, G. P. (2000). The geometry, kinematics and



- 978 rates of deformation within an en échelon normal fault segment bound-  
 979 ary, central Italy. *Journal of Structural Geology*, 22(8), 1027-1047. doi:  
 980 10.1016/S0191-8141(00)00030-4
- 981 Mukul, M., Srivastava, V., Jade, S., & Mukul, M. (2017). Uncertainties in the  
 982 Shuttle Radar Topography Mission (SRTM) Heights: Insights from the In-  
 983 dian Himalaya and Peninsula. *Nature Scientific Reports*, 7(41672). doi:  
 984 10.1038/srep41672
- 985 Nicolosi, I., Speranza, F., & Chiappini, M. (2006). Ultrafast oceanic spreading of  
 986 the Marsili Basin, southern Tyrrhenian Sea: Evidence from magnetic anomaly  
 987 analysis. *Geology*, 34(9), 717-720. doi: 10.1130/g22555.1
- 988 Olivetti, V., Cyr, A. J., Molin, P., Faccenna, C., & Granger, D. E. (2012). Uplift  
 989 history of the Sila Massif, southern Italy, deciphered from cosmogenic <sup>10</sup>Be  
 990 erosion rates and river longitudinal profile analysis. *Tectonics*, 31(3). doi:  
 991 10.1029/2011TC003037
- 992 Palmentola, G., Acquafredda, P., & Fiore, S. (1990). A new correlation of the glacial  
 993 moraines in the Southern Apennines, Italy. *Geomorphology*, 3(1), 1-8. doi: 10  
 994 .1016/0169-555X(90)90028-O
- 995 Pantosti, D., Schwartz, D., & Valensise, G. (1993). Paleoseismology along the 1980  
 996 surface rupture of the Irpinia fault: implications for earthquake recurrence  
 997 in the southern Apennines. *Journal of Geophysical Research: Solid Earth*,  
 998 98(B4), 6561-6577. doi: 10.1029/92JB02277
- 999 Parker, R. L. (1977). Understanding inverse theory. *Annual Review of Earth and*  
 1000 *Planetary Sciences*, 5, 35-64. doi: 10.1146/annurev.ea.05.050177.000343
- 1001 Paul, J. D., Roberts, G. G., & White, N. (2014). The African landscape through  
 1002 space and time. *Tectonics*, 33(6), 898-935. doi: 10.1002/2013TC003479
- 1003 Pezzino, A., Angi, G., Fazio, E., Fiannacca, P., Lo Giudice, A., Ortolano, G., ...  
 1004 De Vuono, E. (2008). Alpine metamorphism in the Aspromonte massif:  
 1005 Implications for a new framework for the southern sector of the Calabria-  
 1006 Peloritani orogen, Italy. *International Geology Review*, 50(5), 423-441. doi:  
 1007 10.2747/0020-6814.50.5.423
- 1008 Piromallo, C., Becker, T., Funicello, F., & Faccenna, C. (2006). Three-dimensional  
 1009 instantaneous mantle flow induced by subduction. *Geophysical Research Let-*  
 1010 *ters*, 33(8), L08304. doi: 10.1029/2005GL025390
- 1011 Piromallo, C., & Morelli, A. (2003). *P* wave tomography of the mantle under the  
 1012 Alpine-Mediterranean area. *Journal of Geophysical Research: Solid Earth*,  
 1013 108(B2), 2065. doi: 10.1029/2002JB001757
- 1014 Pirrotta, C., Barbano, M. S., & Monaco, C. (2016). Evidence of active tectonics in  
 1015 southern Calabria (Italy) by geomorphic analysis: the examples of the Catona  
 1016 and Petrace rivers. *Italian Journal of Geosciences*, 135(1), 142-156. doi:  
 1017 10.3301/IJG.2015.20
- 1018 Pritchard, D., Roberts, G., White, N., & Richardson, C. (2009). Uplift histories  
 1019 from river profiles. *Geophysical Research Letters*, 36(24), L24301. doi: 10  
 1020 .1029/2009GL040928
- 1021 Quye-Sawyer, J., Whittaker, A., & Roberts, G. (2020). Calibrating fluvial erosion  
 1022 laws and quantifying river response to faulting in Sardinia, Italy. *Geomorphol-*  
 1023 *ogy*, 370, 107388. doi: j.geomorph.2020.107388
- 1024 Roberts, G. G., & White, N. (2010). Estimating uplift rate histories from river  
 1025 profiles using African examples. *Journal of Geophysical Research: Solid Earth*,  
 1026 115(B2), B02406. doi: 10.1029/2009JB006692
- 1027 Roberts, G. G., White, N., Hoggard, M. J., Ball, P. W., & Meenan, C. (2018). A  
 1028 Neogene history of mantle convective support beneath Borneo. *Earth and*  
 1029 *Planetary Science Letters*, 496, 142-158. doi: 10.1016/j.epsl.2018.05.043
- 1030 Roberts, G. G., White, N., Martin-Brandis, G., & Crosby, A. (2012). An up-  
 1031 lift history of the Colorado Plateau and its surroundings from inverse  
 1032 modeling of longitudinal river profiles. *Tectonics*, 31(4), TC4022. doi:

- 1033 10.1029/2012TC003107
- 1034 Roberts, G. P., Meschis, M., Houghton, S., Underwood, C., & Briant, R. M.  
1035 (2013). The implications of revised Quaternary palaeoshoreline chronolo-  
1036 gies for the rates of active extension and uplift in the upper plate of sub-  
1037 duction zones. *Quaternary Science Reviews*, 78, 169-187. doi: 10.1016/  
1038 j.quascirev.2013.08.006
- 1039 Roberts, G. P., & Michetti, A. (2004). Spatial and temporal variations in growth  
1040 rates along active normal fault systems: an example from The Lazio – Abruzzo  
1041 Apennines, central Italy. *Journal of Structural Geology*, 26, 339-376. doi:  
1042 10.1016/S0191-8141(03)00103-2
- 1043 Robustelli, G. (2019). Geomorphic constraints on uplift history in the Aspromonte  
1044 Massif, southern Italy. *Geomorphology*, 327, 319-337. doi: 10.1016/j.geomorph  
1045 .2018.11.011
- 1046 Roda-Boluda, D. C., D’Arcy, M., McDonald, J., & Whittaker, A. (2018). Litholog-  
1047 ical controls on hillslope sediment supply: insights from landslide activity and  
1048 grain size distributions. *Earth Surface Processes and Landforms*, 43, 956-977.  
1049 doi: 10.1002/esp.4281
- 1050 Roda-Boluda, D. C., D’Arcy, M., Whittaker, A. C., Gheorghiu, D. M., & Rodés, Á.  
1051 (2019). <sup>10</sup>Be erosion rates controlled by transient response to normal faulting  
1052 through incision and landsliding. *Earth and Planetary Science Letters*, 507,  
1053 140-153. doi: 10.1016/j.epsl.2018.11.032
- 1054 Roda-Boluda, D. C., & Whittaker, A. C. (2017). Structural and geomorpho-  
1055 logical constraints on active normal faulting and landscape evolution in  
1056 Calabria, Italy. *Journal of the Geological Society*, 174(4), 701-720. doi:  
1057 10.1144/jgs2016-097
- 1058 Rodríguez Tribaldos, V., White, N. J., Roberts, G. G., & Hoggard, M. J. (2017).  
1059 Spatial and temporal uplift history of South America from calibrated drainage  
1060 analysis. *Geochemistry, Geophysics, Geosystems*, 18(6), 2321-2353. doi:  
1061 10.1002/2017GC006909
- 1062 Rosenbaum, G., & Lister, G. S. (2004). Neogene and Quaternary rollback evolu-  
1063 tion of the Tyrrhenian Sea, the Apennines, and the Sicilian Maghrebides. *Tec-  
1064 tonics*, 23(1), TC1013. doi: 10.1029/2003TC001518
- 1065 Rosenbaum, G., Lister, G. S., & Duboz, C. (2002). Reconstruction of the tectonic  
1066 evolution of the western Mediterranean since the Oligocene. *Journal of the  
1067 Virtual Explorer*, 8, 107-130. doi: 10.3809/jvirtex.2002.00053
- 1068 Rossetti, F., Faccenna, C., Goffé, B., Monié, P., Argentieri, A., Funicello, R., &  
1069 Mattei, M. (2001). Alpine structural and metamorphic signature of the Sila  
1070 Piccola Massif nappe stack (Calabria, Italy): Insights for the tectonic evolution  
1071 of the Calabrian Arc. *Tectonics*, 20(1), 112-133. doi: 10.1029/2000TC900027
- 1072 Rossetti, F., Goffé, B., Monié, P., Faccenna, C., & Vignaroli, G. (2004). Alpine oro-  
1073 genic P-T-t-deformation history of the Catena Costiera area and surrounding  
1074 regions (Calabrian Arc, southern Italy): The nappe edifice of north Calabria  
1075 revised with insights on the Tyrrhenian-Apennine system formation. *Tectonics*,  
1076 23(6). doi: 10.1029/2003TC001560
- 1077 Rossi, V., Longhitano, S., Mellere, D., Dalrymple, R., Steel, R., Chiarella, D., &  
1078 Olariu, C. (2017). Interplay of tidal and fluvial processes in an early Pleis-  
1079 tocene, delta-fed, strait margin (Calabria, Southern Italy). *Marine and  
1080 Petroleum Geology*, 87, 14-30. doi: j.marpetgeo.2017.02.021
- 1081 Rovida, A. N., Locati, M., Camassi, R. D., Lolli, B., & Gasperini, P. (2016).  
1082 *CPT115, the 2015 version of the Parametric Catalogue of Italian Earthquakes*.  
1083 Istituto Nazionale di Geofisica e Vulcanologia.
- 1084 Royden, L., & Perron, J. T. (2013). Solutions of the stream power equation and ap-  
1085 plication to the evolution of river longitudinal profiles. *Journal of Geophysical  
1086 Research: Earth Surface*, 118(2), 497-518. doi: 10.1002/jgrf.20031
- 1087 Rudge, J. F., Roberts, G. G., White, N. J., & Richardson, C. N. (2015). Uplift

- 1088 histories of Africa and Australia from linear inverse modeling of drainage in-  
 1089 ventories. *Journal of Geophysical Research: Earth Surface*, *120*(5), 894-914.  
 1090 doi: 10.1002/2014JF003297
- 1091 Savelli, C. (2002). Timespace distribution of magmatic activity in the western  
 1092 Mediterranean and peripheral orogens during the past 30 Ma (a stimulus to  
 1093 geodynamic considerations). *Journal of Geodynamics*, *34*(1), 99-126. doi:  
 1094 10.1016/S0264-3707(02)00026-1
- 1095 Schellart, W. (2004). Kinematics of subduction and subduction-induced flow in the  
 1096 upper mantle. *Journal of Geophysical Research*, *109*, B07401. doi: 10.1029/  
 1097 2004JB002970
- 1098 Scicchitano, G., Antonioli, F., Berlinghieri, E. F. C., Dutton, A., & Monaco, C.  
 1099 (2008). Submerged archaeological sites along the Ionian coast of southeast-  
 1100 ern Sicily (Italy) and implications for the Holocene relative sea-level change.  
 1101 *Quaternary Research*, *70*(1), 26-39. doi: 10.1016/j.yqres.2008.03.008
- 1102 Shen, Z., Dawers, N. H., Törnqvist, T. E., Gasparini, N. M., Hijma, M. P., & Mauz,  
 1103 B. (2017). Mechanisms of late Quaternary fault throw-rate variability along  
 1104 the north central Gulf of Mexico coast: implications for coastal subsidence.  
 1105 *Basin Research*, *29*(5), 557-570. doi: 10.1111/bre.12184
- 1106 Siddall, M., Chappell, J., & Potter, E.-K. (2007). 7. Eustatic sea level during past  
 1107 interglacials. In F. Sirocko, M. Claussen, M. F. S. Goñi, & T. Litt (Eds.), *The*  
 1108 *climate of past interglacials* (Vol. 7, p. 75-92). Elsevier. doi: 10.1016/S1571-  
 1109 -0866(07)80032-7
- 1110 Siddall, M., Hönisch, B., Waelbroeck, C., & Huybers, P. (2010). Changes in  
 1111 deep Pacific temperature during the mid-Pleistocene transition and Qua-  
 1112 ternary. *Quaternary Science Reviews*, *29*(1), 170-181. doi: 10.1016/  
 1113 j.quascirev.2009.05.011
- 1114 Sklar, L., & Dietrich, W. E. (1998). River longitudinal profiles and bedrock  
 1115 incision models: Stream power and the influence of sediment supply. In  
 1116 K. Tinkler & E. Wohl (Eds.), *Rivers over rock: Fluvial processes in bedrock*  
 1117 *channels* (Vol. 107, p. 237-260). American Geophysical Union. doi:  
 1118 10.1029/GM107p0237
- 1119 Spina, V., Tondi, E., & Mazzoli, S. (2011). Complex basin development in a wrench-  
 1120 dominated back-arc area: Tectonic evolution of the Crati Basin, Calabria,  
 1121 Italy. *Journal of Geodynamics*, *51*, 90-109. doi: 10.1016/j.jog.2010.05.003
- 1122 Stanley, J., & Bernasconi, M. P. (2012). Buried and submerged Greek archaeo-  
 1123 logical coastal structures and artifacts as gauges to measure late Holocene  
 1124 seafloor subsidence off Calabria, Italy. *Geoarchaeology*, *27*(3), 189-205. doi:  
 1125 10.1002/gea.21405
- 1126 Stock, J. D., & Montgomery, D. R. (1999). Geologic constraints on bedrock river  
 1127 incision using the stream power law. *Journal of Geophysical Research: Solid*  
 1128 *Earth*, *104*(B3), 4983-4993. doi: 10.1029/98JB02139
- 1129 Stucky de Quay, G., Roberts, G., Watson, J., & Jackson, C. (2017). Incipient  
 1130 mantle plume evolution: Constraints from ancient landscapes buried beneath  
 1131 the North Sea. *Geochemistry, Geophysics, Geosystems*, *18*(3), 973-993. doi:  
 1132 10.1002/2016GC006769
- 1133 Tarboton, D. G. (1997). A new method for the determination of flow directions  
 1134 and upslope areas in grid digital elevation models. *Water Resources Research*,  
 1135 *33*(2), 309-319. doi: 10.1029/96WR03137
- 1136 Tortorici, L., Monaco, C., Tansi, C., & Cocina, O. (1995). Recent and active tecton-  
 1137 ics in the Calabrian arc (Southern Italy). *Tectonophysics*, *243*(1), 37-55. doi:  
 1138 10.1016/0040-1951(94)00190-K
- 1139 Westaway, R. (1993). Quaternary Uplift of Southern Italy. *Journal of Structural Ge-*  
 1140 *ology*, *98*(B12), 21741-21772. doi: 10.1029/93JB01566
- 1141 Westaway, R., & Bridgland, D. (2007). Late Cenozoic uplift of southern Italy  
 1142 deduced from fluvial and marine sediments: Coupling between surface pro-

- 1143 cesses and lower-crustal flow. *Quaternary International*, 175, 86-124. doi:  
 1144 10.1016/j.quaint.2006.11.015
- 1145 Whipple, K. X. (2004). Bedrock rivers and the geomorphology of active oro-  
 1146 gens. *Annual Review of Earth and Planetary Science*, 32, 151-185. doi:  
 1147 10.1146/annurev.earth.32.101802.120356
- 1148 Whipple, K. X., & Tucker, G. E. (1999). Dynamics of the stream-power river in-  
 1149 cision model: Implications for height limits of mountain ranges, landscape  
 1150 response timescales, and research needs. *Journal of Geophysical Research:*  
 1151 *Solid Earth*, 104 (B8), 17661-17674. doi: 10.1029/1999JB900120
- 1152 Whittaker, A. C. (2012). How do landscapes record tectonics and climate? *Litho-*  
 1153 *sphere*, 4(2), 160-164. doi: 10.1130/RF.L003.1
- 1154 Whittaker, A. C., & Boulton, S. J. (2012). Tectonic and climatic controls on knick-  
 1155 point retreat rates and landscape response times. *Journal of Geophysical Re-*  
 1156 *search: Earth Surface*, 117(F2), F02024. doi: 10.1029/2011JF002157
- 1157 Whittaker, A. C., Cowie, P. A., Attal, M., Tucker, G. E., & Roberts, G. P. (2007).  
 1158 Contrasting transient and steady-state rivers crossing active normal faults:  
 1159 new field observations from the Central Apennines, Italy. *Basin Research*,  
 1160 19(4), 529-556. doi: 10.1111/j.1365-2117.2007.00337.x
- 1161 Whittaker, A. C., & Walker, A. S. (2015). Geomorphic constraints on fault  
 1162 throw rates and linkage times: Examples from the Northern Gulf of Evia,  
 1163 Greece. *Journal of Geophysical Research: Earth Surface*, 120(1), 137-158. doi:  
 1164 10.1002/2014JF003318
- 1165 Willett, S. D., McCoy, S. W., Perron, J. T., Goren, L., & Chen, C.-Y. (2014). Dy-  
 1166 namic reorganization of river basins. *Science*, 343(6175), 1248765. doi: 10  
 1167 .1126/science.1248765
- 1168 Wobus, C., Whipple, K., Kirby, E., Snyder, N., Johnson, J., Spyropolou, K., ...  
 1169 Sheehan, D. (2006). Tectonics from topography: Procedures, promise, and  
 1170 pitfalls. In S. Willett, N. Hovius, M. Brandon, & D. Fisher (Eds.), *Tectonics,*  
 1171 *climate, and landscape evolution: Geological society of america special paper*  
 1172 *398* (p. 55-74). Geological Society of America. doi: 10.1130/2006.2398(04)
- 1173 Wortel, M., & Spakman, W. (2000). Subduction and slab detachment in the  
 1174 Mediterranean-Carpathian region. *Science*, 290(5498), 1910-1917. doi:  
 1175 10.1126/science.290.5498.1910
- 1176 Zandt, G., & Humphreys, E. (2008). Toroidal mantle flow through the western U.S.  
 1177 slab window. *Geology*, 36(4), 295-298. doi: 10.1130/G24611A.1
- 1178 Zecchin, M., Nalin, R., & Roda, C. (2004). Raised Pleistocene marine terraces  
 1179 of the Crotona peninsula (Calabria, southern Italy): facies analysis and or-  
 1180 ganization of their deposits. *Sedimentary Geology*, 172(12), 165-185. doi:  
 1181 10.1016/j.sedgeo.2004.08.003
- 1182 Zhu, C., Byrd, R. H., Lu, P., & Nocedal, J. (1997). Algorithm 778: L-BFGS-B:  
 1183 Fortran subroutines for large-scale bound-constrained optimization. *ACM*  
 1184 *Transactions on Mathematical Software (TOMS)*, 23(4), 550-560. doi:  
 1185 10.1145/279232.279236
- 1186 Zondervan, J. R., Whittaker, A. C., Bell, R. E., Watkins, S. E., Brooke, S. A., &  
 1187 Hann, M. G. (2020). New constraints on bedrock erodibility and landscape  
 1188 response times upstream of an active fault. *Geomorphology*, 351, 106937. doi:  
 1189 10.1016/j.geomorph.2019.106937